ELSEVIER

Tectonophysics 253 (1996) 167–208

TECTONOPHYSICS

Constraints on present-day plate motions south of 30°S from satellite altimetry

Sharon Spitzak, Charles DeMets *

Department of Geology and Geophysics University of Wisconsin at Madison, Madison, Wisconsin, USA

Received 14 November 1994; accepted 12 June 1995

Abstract

Gridded free-air gravity anomalies derived from Geosat and Seasat altimetric observations are used to locate all mid-ocean ridge transform faults south of 30°S, and wherever possible, assign azimuths and uncertainties useful for plate kinematic analysis. A total of 131 ridge offsets longer than 30 km were located, of which 114 are clearly transform faults with well-defined valleys. Azimuthal uncertainties range from 0.6° for the longest transform faults to nearly 10° for the transform faults with lengths close to 30 km. To assess whether the altimetrically-derived azimuths are representative of present-day plate slip directions, azimuths of transform faults mapped with side-scan sonar and side-looking or conventional bathymetric systems were compared to their altimetrically-derived counterparts. Comparison of these two independently-estimated sets of azimuths using the χ^2 test shows no significant difference, indicating that the altimetrically-derived azimuths can be used where bathymetrically-derived azimuths are not available. We also find no evidence that large age-offset transform faults are less representative of present-day slip directions than short age-offset transforms. Models constructed using the altimetrically-derived azimuths fit the NUVEL-1 spreading rates, transform azimuths, and earthquake slip vectors nearly as well as NUVEL-1, as well as decreasing the model uncertainties. Thus, the altimetrically-derived azimuths offer improved accuracy and decreased uncertainties in estimates of global plate velocities without increasing non-closures of plate circuits beyond the level already present in NUVEL-1. In practical terms, plate velocities predicted by models that substitute the altimetrically-derived azimuths for all NUVEL-1 transform azimuths from below 30°S never differ from velocities predicted by NUVEL-1 by more than 0.3 mm yr^{-1} and 4°; however, the several-degree azimuthal misfits to altimetrically-derived azimuths from the Africa–Antarctic and Pacific–Antarctic plate boundaries are statistically significant and suggest there are several-degree inaccuracies in the predictions of the NUVEL-1 angular velocities. The new catalog of southern hemisphere transform fault azimuths should prove useful for at least the following: (1) improvement of models of deformation of the Australian plate west of the Macquarie Ridge Complex; (2) improvement of estimates of motion between the Australian and Pacific plates; (3) revision of upward bounds on the amount of seafloor deformation south of Africa related to rifting of the African plate; and (4) studies of a possible deforming zone within the South American plate east of the South Sandwich trench.

* 1215 W Dayton St., Dept of Geology and Geophysics, U.W.-Madison, Madison, WI 53706, USA, Fax: +1 608-262-0693, E-mail: chuck@geology.wisc.edu

SSDI 0040-1951(95)00069-0

1. Introduction

To a large degree, the accuracy of models of present-day plate motions depends on the availability of well-determined spreading rates and azimuths of transform faults along mid-ocean ridges. For instance, nearly 90% of the kinematic information underlying the NUVEL-1 model for 3.0 m.y.-average global plate motions is derived from seafloor spreading rates and the strikes of transform faults that offset ridge segments (DeMets et al., 1990). In contrast, earthquake slip vectors, though comprising the majority of available kinematic data, have little practical effect on the ability to predict present-day plate velocities (DeMets, 1993). Further improvements in models of plate velocities averaged over the past several million years are thus most likely to come from the addition of well-determined spreading rates and transform fault azimuths, particularly from spreading centers currently underrepresented in plate motion data sets.

The most poorly represented plate boundaries in the NUVEL-1 data set are the spreading centers south of 30°S, where geographic remoteness and inclement weather have impeded ship-board surveys. Although over 36,000 of the 86,000 + km-long mid-ocean ridge system (over 40%) lies below 30°S, spreading rates and transforms from these sparsely surveyed spreading centers contribute less than 20% of the total data importance in NUVEL-1. The dearth of high-quality ship-board observations in this region is particularly unfortunate because the five spreading centers separating Antarctica from the adjacent African, Australian, Nazca, Pacific, and South American plates are an integral part of the global plate circuit and contain important information regarding topics such as: possible non-rigidity of the Australian plate near the Macquarie triple junction (e.g., the meeting point of the Australian, Antarctic, and Pacific plates) (DeMets et al., 1988; Valenzuela and Wysession, 1993), possible slow deformation of seafloor south of Africa related to the East African Rift (Mougenot et al., 1986; Hartnady, 1990; Jestin et al., 1994), and non-closures of the Australia–Africa–Antarctica (DeMets et al., 1994a) and Africa–South America–Antarctica (DeMets et al., 1990) plate circuits.

Many of these problems can now be revisited due to the recent release of previously classified, closely spaced satellite altimetric profiles from the Geosat Geodetic Mission (GM) (Marks et al., 1993). The marine geoid extracted from Geosat GM data has for the first time defined details of the southern ocean basin spreading centers, including the ridge-transform configuration necessary for studies of present-day plate kinematics. The considerable improvement in the marine geoid stems largely from the dramatically reduced distance between the flight paths of both ascending and descending satellite tracks where they cross the equator. Track spacings for the Geosat GM data are ~ 5 km, approximately 10 times closer than for previously released Seasat and Geosat Exact Repeat Mission (ERM) data.

Our goal here is to demonstrate that information contained in altimetric data regarding locations, azimuths, and lengths of oceanic transform faults can be used to improve models of present-day plate velocities. We begin by demonstrating that altimetrically-derived azimuths agree within their estimated uncertainties with azimuths determined from detailed acoustic surveys of transform faults, which are widely accepted as accurate measures of present-day slip directions. We next compare the newly derived azimuths along each of the six spreading centers located south of 30°S to directions predicted by NUVEL-1 in order to determine the regions where the new azimuths provide new information. Finally, we undertake a rigorous comparison of the fits of several alternative closure-enforced global plate motion models to both the altimetrically-derived azimuths and other data such as spreading rates used to derive these models. Our intention is to determine whether the altimetrically-derived azimuths might be one of several reasons to produce a new global plate motion model in the near future.

2. Data analysis and reduction

Two types of data are used here to estimate transform fault azimuths: gridded, free-air gravity anomalies derived from satellite altimetric measurements, and acoustic measurements of transform valley depths and seafloor backscatter from precision

depth recorders, bathymetric swath mapping systems such as Seabeam, side-scan sonar systems such as GLORIA, and systems such as SeaMarc that combine the latter two techniques. For lack of a more suitable term, azimuths derived using direct measurements of seafloor properties such as bathymetry and backscatter are hereafter referred to as "bathymetrically-derived". Bathymetrically-derived azimuths are used here as the standard of comparison for altimetrically-derived azimuths.

As with prior analyses of satellite altimetry for the purposes of constructing models of past plate motions (e.g., Gahagan et al., 1988; Mayes et al., 1990; Royer and Sandwell, 1989), we assume that marine gravity anomalies with wavelengths less than ~ 200 km are caused primarily by uncompensated seafloor topography. In support of this assumption, Neumann et al. (1993) has demonstrated that the gridded free-air gravity field derived from Geosat GM and ERM tracks over the southern Atlantic is coherent with seafloor bathymetry down to 2-D spatial wavelengths of ~ 26 km. The marine gravity field in this region thus is an excellent proxy for seafloor bathymetry, including transform faults. The loss of coherence for 2-D wavelengths less than ~ 26 km limits our ability to image transform faults shorter than this. Fortunately, little if any plate kinematic information is lost because true transform faults, which are defined by Searle (1986) as bands of throughgoing strike-slip faults, do not appear to form consistently until ridge offsets exceed 25–30 km (Searle, 1986).

In the ensuing analysis, we define the relative slip direction between two plates as follows. For high resolution observations of transform fault valleys (e.g., from GLORIA, Seabeam, or SeaMarc), which are capable of imaging transform fault traces and scarps, strike-slip features within the transform valley are assumed to parallel the present slip direction. For lower resolution observations (e.g., altimetry or conventional bathymetry), which cannot resolve fault traces within a transform valley, strike-slip motion is assumed to parallel the transform valley. Although the ensuing analysis suggests that strike-slip motion generally parallels the trend of transform fault valleys, multi-beam observations clearly demonstrate that strike-slip motion sometimes occurs along a series of nearly parallel faults connected by extensional or compressional relay zones, with an overall fault arrangement that is oblique to the trend of the valley (Fox and Gallo, 1989 and see fig. 6 in Garfunkel (1986)). This is an important and seemingly unavoidable source of error in altimetrically-derived estimates of transform fault slip directions, and must be considered when analyzing the reasons for data outliers.

2.1. Altimetric data

The gridded free-air gravity anomalies used here were derived from Seasat, Geosat ERM, and Geosat GM altimetric measurements of sea surface height south of 30°S (Marks et al., 1993). The nearly 7 million gridded marine gravity observations are spaced by 0.04° in latitude and 0.05° in longitude, reflecting the along-track sampling interval of ~ 3–4 km and the ~ 5-km spacing between the Geosat GM tracks (Sandwell, 1992). The gridded data used here are available from NOAA through the National Geophysical Data Center (NGDC Data Announcement 93-MGG-01, Global Relief Data on CD-ROM, 1993).

2.2. Bathymetric and side-scan sonar data

To find high-quality bathymetrically-derived transform azimuths, we searched the literature and solicited colleagues for information regarding transform faults located south of 30°S. Ultimately, we found 29 transform faults, 13 of which had been mapped using multi-beam echo-sounding arrays, side-scan sonar, or both, and 16 of which had been mapped with at least 5–10 conventional bathymetric transects (Table 1). Slip directions for the former subset were determined by visually fitting linear trends to sinuous fault strands or networks of connected lineaments within the transform valley; slip directions for the latter were assumed to parallel the transform fault valley. As described in the appendix, uncertainties assigned to individual azimuths depend on the length of the well-surveyed portion of the transform fault and the width of the imaged zone of active faulting, ranging from the entire transform valley for low resolution measurements to the much narrower transform tectonised zone and principal transform displacement zone for high resolution measurements (Searle, 1986; Fox and Gallo, 1989).

2.3. Estimating transform fault locations, azimuths, and uncertainties

The appendix describes how we estimated the locations, azimuths, and azimuthal uncertainties of transform faults south of 30°S. Briefly, we created three sets of large-scale maps, one of which displayed the free-air gravity signature, and the second and third of which showed the gravitational gradients computed for the directions orthogonal and parallel to the local transform fault azimuths, respectively. We then interpreted and digitized the plate boundary configuration, and estimated the azimuths and uncertainties for all ridge offsets longer than 30 km.

Fig. 1 demonstrates the good agreement between the ridge-transform configuration suggested by the altimetric data and that defined by SeaMarc II sidescan sonar and bathymetric observations of a ~ 350-km stretch of the Southeast Indian Ridge (Sempéré et al., 1991). The ridge segments and their offsets

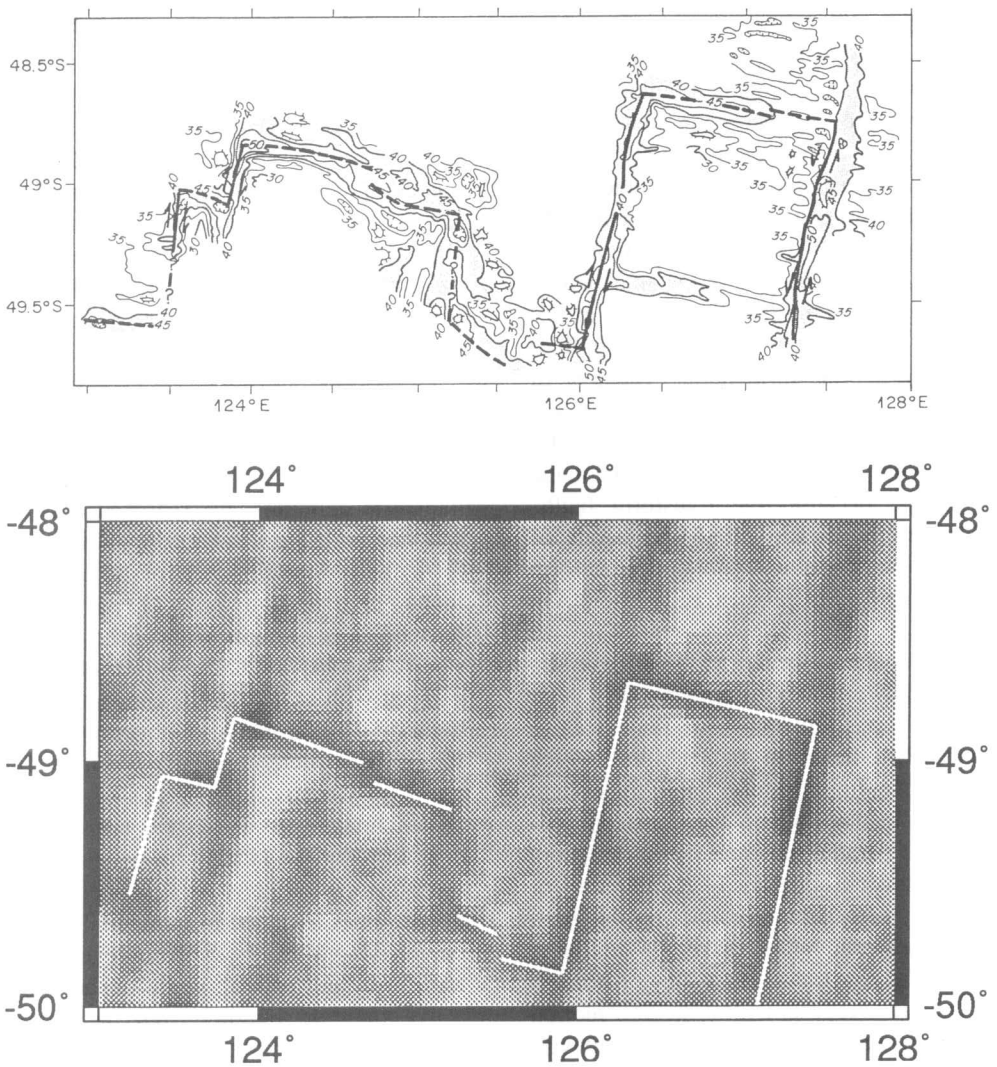

Fig. 1. Upper: Ridge-transform configuration determined from a SeaMarc II swath-mapping survey of a section of the Southeast Indian Ridge (adapted from Sempéré et al., 1991). Lower: Plate boundary determined from the gridded free-air gravity anomalies derived from Seasat and Geosat altimetry for the same section of the ridge.

interpreted from the altimetric data agree remarkably well (though not perfectly) with those defined from the SeaMarc II observations, even for ridge offsets as short as 10 km (see for example the ridge offset at 49.8°S, 125.5°E). Similar good agreements were observed in several other areas where bathymetric observations were dense enough to define the plate boundary [e.g., the Southwest Indian Ridge from 21° to 23°E and the Pacific–Antarctic rise northeast of the Eltanin fracture zone (Lonsdale, 1994)]. In general, interpretation of the ridge-transform configuration was straightforward — we would be happy if all geophysical data sets were equally unambiguous. Our complete interpretation is shown in the Appendix (Figs. 6–24).

There were several areas where the plate boundary configuration was not defined unambiguously by the altimetry. From 10°E to 14°E along the Southwest Indian Ridge, the plate boundary is defined by a wide gravity low whose orientation is highly oblique to the expected opening direction (Appendix 1, Fig. 6). Several NE-trending gravity lineations that are enhanced by taking the directional derivative of the gravity field (lower panel of Appendix 1, Fig. 6) may be fracture zones, which implies that several transform faults offset the spreading center from 10°–14°E. We have thus interpreted the plate boundary as a series of short ridge segments and transform faults. The locations of ridge segments and transform faults from 54°–56°E along the Southwest Indian Ridge were also hard to determine (Appendix 4, Fig. 9). Two NE-trending free-air gravity lows appear to define the plate boundary; however, it is unclear whether these obliquely trending features are products of constructive interference between the gravity lows associated with the transform fault valleys and short axial valleys, or are instead narrow zones of highly oblique spreading such as those mapped by a high-resolution GLORIA survey of the spreading center in the western Gulf (Tamsett and Searle, 1988). We adopted a ridge-transform configuration similar to that proposed de Ribet and Patriat (1988), who based their interpretation on ship-board magnetic and bathymetric observations. Along the Southeast Indian Ridge, the configuration of the plate boundary at 78°E from 37°–41°S (Appendix 5, Fig. 10) is masked by the volcanic edifices of the nearby Amsterdam and Saint Paul islands. Our interpretation depends partly on that of Royer and Schlich (1988), who synthesized the regional bathymetric and magnetic observations. Finally, the spreading center west of the Australia–Antarctic discordance (Appendix 7, Fig.12) is offset by several short transform faults whose azimuths are poorly defined by the altimetry. At least some of these offsets appear to be related to a series of propagating rifts that appear to follow the bathymetric gradient leading into the zone of presumed mantle downwelling beneath the Australia–Antarctic discordance (Marks et al., 1990; Kuo, 1993; Morgan and Sandwell, 1994).

Because of the ambiguities involved in defining ridge-transform configurations in the regions described above, we believe that any azimuths taken from the interpreted plate boundary configurations are likely to be influenced strongly by individual prejudices and are therefore unsuitable for use in a quantitative analysis such as this. All plate boundary features from these regions are thus excluded from further consideration here.

Fig. 2 shows our interpretation of the spreading centers south of 30°S; a file containing the digitized coordinates is available upon request. Table 1 lists the mid-points, lengths, azimuths, and estimated uncertainties for 114 transform faults longer than 30 km whose azimuths we believe are reliable. These transforms, which represent a nearly complete catalog of transform faults below 30°S, represent a considerable increase over the 56 transform fault azimuths below 30°S in the NUVEL-1 data set. The catalog is not yet complete due to the previously mentioned ambiguities in ridge-transform configurations in some regions.

Two likely sources of random error contribute to the uncertainties we determined for the 114 transform fault azimuths. The principal uncertainty comes from our ignorance of the location and azimuth of the active fault(s) within the transform valley. Where strike-slip motion is accommodated by a single fault or series of faults that extend the entire length of the valley, the uncertainty is a simple function of the measured length and width of the transform fault valley (this is further described in the appendix). Lengths of transform valleys are easily measured, but widths of the transform valleys vary from as few as several km to several tens of kilometers and are more difficult to estimate using gravity data. We thus

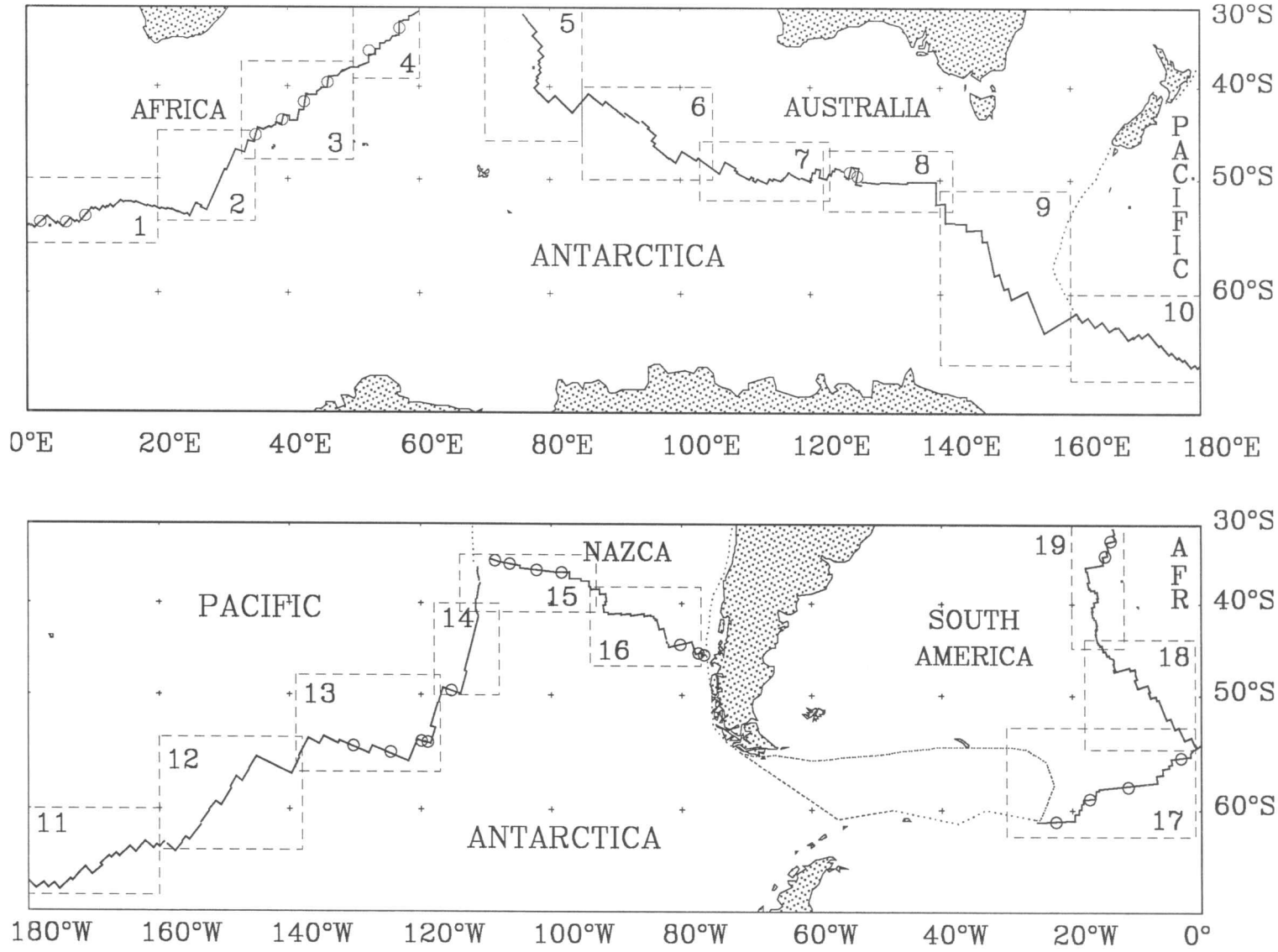

Fig. 2. Spreading centers below 30°S interpreted from altimetry (solid lines). Dotted lines show other plate boundaries. Open circles designate transform faults whose azimuths were estimated using bathymetric or side-scan sonar surveys. The inset maps outlined by dashed lines and their associated numbers correspond to figures shown in the appendix. Projection is Mercator.

Table 1
Transform fault information

Mid-point of transform		From Altimetry			From Bathymetry †		
Latitude (°N)	Longitude (°E)	Length (km)	Azimuth (°CW)	σ	Azimuth	σ	Source
Southwest Indian Ridge							
−54.16	2.17	170	46.5	1.6	44.5	1.7	1
−54.21	6.05	113	43.0	2.4	40.0	10.6	2
−53.54	8.89	196	41.0	1.4	39.0	1.9	2
−52.98	25.43	151	25.5	1.8	–	–	–
−51.06	29.00	480	24.5	0.7	–	–	–
−48.11	31.33	261	23.0	1.1	–	–	–
−46.70	33.67	149	14.5	1.8	–	–	–
−45.46	35.10	172	15.0	1.6	17.0	0.9	3
−43.82	39.18	110	12.5	2.4	13.0	2.7	3
−43.66	40.28	52	0.0	5.0	–	–	–
−43.32	41.61	136	8.5	2.0	–	–	–
−41.82	42.56	210	8.5	1.3	08.0	1.7	3
−40.80	44.42	36	15.0	7.3	–	–	–
−39.49	46.11	145	7.5	1.9	03.0	7.8	3
−36.65	52.32	111	0.0	2.4	04.0	2.5	3
−35.84	53.40	68	1.5	3.9	–	–	–
−34.98	54.12	52	1.0	5.0	–	–	–
−32.74	56.99	206	0.0	1.3	00.5	0.5	4
−31.40	58.39	60	3.5	4.4	–	–	–
Southeast Indian Ridge							
−33.43	77.65	90	46.5	3.0	–	–	–
−35.32	78.51	78	45.0	3.4	–	–	–
−36.62	78.67	94	46.0	2.8	–	–	–
−41.41	80.33	121	44.5	2.2	–	–	–
−41.91	84.72	319	41.5	0.9	–	–	–
−41.92	88.37	59	37.5	4.5	–	–	–
−45.71	95.93	79	37.0	3.4	–	–	–
−46.40	96.05	34	34.5	7.7	–	–	–
−47.71	99.72	146	28.5	1.8	–	–	–
−47.93	102.51	31	27.0	8.3	–	–	–
−48.82	106.47	146	26.5	1.8	–	–	–
−49.72	120.19	104	13.5	2.6	–	–	–
−49.09	120.78	49	14.0	5.3	–	–	–
−49.37	121.48	86	10.0	3.1	–	–	–
−49.30	123.29	55	15.5	4.8	–	–	–
−48.96	123.78	33	15.0	7.8	–	–	–
−49.28	126.12	136	13.0	2.0	13.0	0.7	5
−49.64	127.25	176	12.0	1.5	10.0	1.2	5
−51.28	139.39	238	1.0	1.2	–	–	–
−53.17	140.77	198	−1.0	1.4	–	–	–
−54.47	144.04	65	−4.5	4.1	–	–	–
−55.21	146.36	117	−7.0	2.3	–	–	–
−57.13	147.72	328	−12.5	0.9	–	–	–
−59.03	149.35	137	−17.5	2.0	–	–	–
−59.95	150.60	102	−16.0	2.6	–	–	–
−61.33	154.54	369	−21.5	0.8	–	–	–

Tabe 1 (continued)

Mid-point of transform		From Altimetry			From Bathymetry †		
Latitude (°N)	Longitude (°E)	Length (km)	Azimuth (°CW)	σ	Azimuth	σ	Source
Pacific–Antarctic Rise							
−61.74	161.32	84	−38.0	3.2	–	–	–
−62.08	163.19	95	−37.5	2.8	–	–	–
−62.39	165.35	94	−40.0	2.8	–	–	–
−62.86	168.06	128	−38.0	2.1	–	–	–
−63.02	170.64	38	−38.0	6.9	–	–	–
−63.28	172.69	130	−41.5	2.1	–	–	–
−63.98	174.47	98	−39.0	2.7	–	–	–
−64.38	175.87	62	−43.0	4.3	–	–	–
−64.60	176.91	40	−42.0	6.5	–	–	–
−64.90	178.01	78	−39.5	3.4	–	–	–
−65.08	179.30	32	−44.5	8.1	–	–	–
−65.32	180.58	89	−47.0	3.0	–	–	–
−65.40	182.70	50	−40.5	5.2	–	–	–
−65.46	184.31	54	−41.0	4.9	–	–	–
−64.46	189.20	76	−44.0	3.5	–	–	–
−63.01	195.91	63	−46.5	4.2	–	–	–
−62.67	198.47	85	−49.5	3.1	–	–	–
−62.87	201.76	87	−52.0	3.0	–	–	–
−62.22	204.35	37	−51.0	7.1	–	–	–
−59.59	209.10	56	−53.5	4.7	–	–	–
−57.62	212.29	68	−55.0	3.9	–	–	–
−56.48	217.56	365	−63.0	0.8	–	–	–
−54.33	223.70	127	−65.0	2.1	–	–	–
−54.22	226.30	159	−65.0	1.7	–	–	–
−54.78	229.74	296	−69.0	1.0	−68.0	0.8	6
−55.33	235.35	380	−71.0	0.8	−70.0	0.5	7
−54.34	240.03	93	−72.0	2.9	−71.0	0.8	7
−54.44	240.96	68	−72.5	3.9	−72.0	1.4	7
−53.08	241.81	49	−72.5	5.3	–	–	–
−49.55	244.67	206	−72.0	1.3	−75.0	1.8	7
Chile Rise							
−34.76	251.31	118	107.5	2.3	106.0	1.5	8
−35.20	253.60	285	100.5	1.0	98.0	2.1	9
−35.98	257.77	466	97.5	0.7	96.0	1.9	9
−36.23	261.64	214	90.0	1.3	92.0	2.0	9
−37.04	263.73	155	89.5	1.7	–	–	–
−37.31	265.23	109	90.5	2.5	–	–	–
−38.32	266.81	100	86.5	2.7	–	–	–
−38.92	267.90	76	84.5	3.5	–	–	–
−40.20	268.17	30	79.5	8.5	–	–	–
−41.06	268.42	51	84.0	5.1	–	–	–
−41.21	269.77	167	85.5	1.6	–	–	–
−41.28	271.48	117	85.5	2.3	–	–	–
−41.35	273.23	173	82.0	1.6	–	–	–
−41.45	274.78	81	81.0	3.3	–	–	–
−41.49	275.50	34	82.5	7.6	–	–	–
−42.95	276.89	53	80.5	5.0	–	–	–
−44.68	279.78	283	78.5	1.0	78.0	0.8	10
−45.65	282.56	77	75.5	3.4	73.0	0.9	10
−45.85	283.45	40	74.0	6.5	73.0	0.9	10

Table 1 (continued)

Mid-point of transform		From Altimetry			From Bathymetry †		
Latitude (°N)	Longitude (°E)	Length (km)	Azimuth (°CW)	σ	Azimuth	σ	Source
American–Antarctic Rise							
−60.87	337.50	320	90.0	0.9	89.0	1.2	11
−60.28	340.76	35	81.0	7.5	–	–	–
−59.12	342.67	102	85.0	2.6	88.0	3.7	11
−58.15	348.64	529	88.0	0.6	84.0	0.9	11
−57.20	353.46	65	81.5	4.1	–	–	–
−56.61	354.39	65	81.5	4.1	–	–	–
−55.73	356.76	195	84.5	1.4	83.0	1.6	11
Southern Mid-Atlantic Ridge							
−32.21	346.01	125	77.0	2.2	78.0	1.1	12
−34.11	345.09	69	77.0	3.8	78.0	1.9	13
−35.36	343.45	251	81.5	1.1	–	–	–
−38.32	343.19	53	80.5	5.0	–	–	–
−39.73	343.67	59	77.0	4.5	–	–	–
−40.28	343.27	39	73.5	6.7	–	–	–
−47.34	347.70	184	75.0	1.5	–	–	–
−47.32	349.33	51	75.0	5.2	–	–	–
−49.08	350.88	118	73.0	2.3	–	–	–
−50.12	352.44	58	74.5	4.6	–	–	–
−52.24	354.86	41	72.5	6.4	–	–	–
−53.09	356.09	47	66.5	5.6	–	–	–
−54.05	357.86	72	66.0	3.7	–	–	–

† Includes azimuths estimated from conventional bathymetry, multi-beam swath mapping bathymetry, or side-scan sonar.Source: 1 = le Roex et al. (1982); 2 = Sclater et al. (1978); 3 = Fisher and Sclater (1983); 4 = Dick et al. (1991); 5 = Palmer et al. (1993); 6 = Lonsdale (1986); 7 = Lonsdale (1994); 8 = Kleinrock and Bird (1994); 9 = Anderson-Fontana et al. (1987); 10 = G. Westbrook (pers. commun., 1994); 11 = Barker and Lawver (1988); 12 = Grindlay et al. (1991); 13 = Fox et al. (1991).

adopted a standard width of 10 km and treated this width as an adjustable parameter, as described below. A second, smaller source of random error is introduced during the process of digitizing the interpreted plate boundary configuration. This is a small part of the total uncertainty, but is included for completeness.

We also investigated an additional potential source of uncertainty, namely, that transform faults with large seafloor age-offsets might not parallel present-day slip directions because transform valley morphologies result from plate-boundary slip over a period equal to the age offset of the transform fault, which in some instances can be more than 50 m.r. For this reason, large age-offset fracture zones are often not used for plate reconstructions (e.g., Patriat, 1985; Royer and Chang, 1991). Studies of present-day plate velocities (e.g., Minster and Jordan, 1978; DeMets et al., 1990) have not previously assessed the possibility that large age-offset transform faults might be unsuitable for estimating present-day plate slip directions; therefore, we examined whether there is any evidence for systematic differences between azimuths estimated from large and small age-offset transform faults, and whether there is a need to downweight or discard azimuths of large age-offset transform faults. Details of this analysis are in the appendix because we did not find any compelling evidence for treating large and small age-offset transform faults differently.

2.4. Calibrating the assigned uncertainties

The procedure for assigning azimuthal uncertainties (described in the appendix) ensures that the uncertainties assigned to the transform faults are relatively correct, but does not guarantee that all of the uncertainties have not been systematically over-

or underestimated. The accuracy of the absolute sizes of the uncertainties depends on the correctness of the following two assumptions: (1) that transform fault valleys are ~ 10 km wide, and (2) that the probability of observing any particular azimuth within the geometrically-permitted range is governed by an equal probability distribution rather than a Gaussian or other distribution. To the degree that one or both of these two assumptions is wrong, the assigned uncertainties will be systematically too large or small.

Fortunately, the dispersion of the azimuths around their most probable value can be used as a guide for recalibrating the initially assigned uncertainties so that they are approximately correct. The most probable value of a transform fault azimuth along a plate boundary is the azimuth predicted by an angular velocity that minimizes the weighted least-squares misfit to azimuths and spreading rates from that plate boundary. Hereafter, this angular velocity will be referred to as a best-fitting angular velocity, and will be abbreviated "BFV". Angular velocities, which are vectors commonly used to describe instantaneous plate rotations, are completely described by three parameters, latitude, longitude, and angular rotation rate. Of these three parameters, azimuthal data such as transform fault azimuths and earthquake slip vectors can constrain at most two (the pole latitude and longitude), and frequently constrain fewer than two parameters if spreading rates also help to constrain the pole location.

The least-squares misfit χ^2 is defined as:

$$\chi^2 = \sum_{i=1}^{N} \left(\frac{d_i^{obs} - d_i^{pred}}{\sigma_i} \right)^2 \qquad (1)$$

where d_i^{pred} is the value of the ith datum predicted by the model, d_i^{obs} is the observed azimuth, and σ_i is the standard error assigned to the observed azimuth. The expectation value for the fraction of χ^2 related to a misfit to N transform faults is $N - m$, where m is the number of adjustable parameters constrained by the N transform faults. Since χ^2 depends on σ_i, the degree to which χ^2 approximates its expectation value depends on how well the assigned uncertainties approximate the true uncertainties. If we define the average misfit in terms of reduced chi-square χ_v^2, where $\chi_v^2 = \chi^2/(N - m)$, then values of χ_v^2 significantly greater or less than 1.0 indicate that uncertainties are systematically over- or underestimated by a factor of $1/\sqrt{\chi_v^2}$.

For each of the six spreading centers partly or entirely below 30°S, we inverted the altimetrically-derived transform azimuths along with 3.0-m.y.-average spreading rates taken from the NUVEL-1 data set to find the BFV and the dispersion of the observed azimuths relative to its predictions [see DeMets et al. (1990) for further details regarding the inversion process]. Four transform faults from the Southeast Indian Ridge just west of the Macquarie triple junction were excluded from this stage of the analysis due to the possibility that these azimuths may not record Australia–Antarctic motion (DeMets et al., 1988). Reduced chi-square for the remaining 110 transform faults ranged from 0.32 to 1.38 for the six spreading centers, with a cumulative value of $\chi_v^2 = 0.66$. The uncertainties we initially assigned to the azimuths were thus overestimated (on average) by a factor of $1/\sqrt{0.66}$ or ~ 1.2, suggesting that either the 10-km width assigned to all transform valleys resulted in too wide a range of geometrically-permitted azimuths, or that our assumption of an equal probability distribution was incorrect. The data do not permit us to distinguish between these two explanations; however, the final, recalibrated uncertainties are nearly the same regardless of which assumption is modified. We thus iteratively adjusted the width of the transform valleys until we found the integer width that yielded reduced chi-square closest to 1.0. A transform valley width of 8 km yielded $\chi_v^2 = 1.00$.

All uncertainties listed in Table 1 have thus been determined from geometrically-defined uncertainties that assume a transform valley width of 8 km combined in quadrature with a $\pm 0.36°$ uncertainty introduced during digitization (see Appendix). We do not attach any physical meaning to the computed valley width of 8 km because adjusting this parameter is merely a convenient way of properly scaling the assigned uncertainties.

We were not able to adjust the uncertainties assigned to the azimuths estimated from bathymetry because none of the spreading centers were populated with enough well-surveyed transform faults to yield a meaningful measure of the dispersion of the azimuths about the predictions of a BFV. However, the estimated uncertainties should be approximately

correct because we directly measured the widths of the zones of active strike-slip faulting in order to compute the geometrically-permitted uncertainties, which was not possible for the altimetrically-imaged transform faults.

3. Comparison to bathymetrically-derived transform azimuths

To determine whether altimetrically-derived transform fault azimuths can be used as reliable measures of present-day slip directions, we compared them to azimuths determined from ship-board bathymetry and sidescan sonar, which provide accurate and precise estimates of azimuths of seafloor features such as transform faults. The χ^2 test (Bevington and Robinson, 1992) provides a suitable way to determine whether the azimuths of transform faults that have been mapped by both bathymetric and altimetric means are drawn from different parent populations. χ^2 is defined as in (1); however, the denominator σ_i must be re-defined as the square root of the sum of the squares of the uncertainties estimated for the altimetrically- and bathymetrically-based azimuths, and the observed and predicted values are defined as the bathymetrically- and altimetrically-derived azimuths, respectively.

Comparison of the 29 bathymetrically-derived azimuths (discussed above) and their altimetric counterparts yields $\chi^2 = 28.0$, significantly less than the value of $\chi^2 = 42.6$ that would indicate a difference significant at the 95% confidence level. The mean residual difference for the 29 paired measurements is 0.2 standard deviations, corresponding to a weighted average difference of only 0.7°. The maximum observed angular difference between these two independently estimated sets of azimuths is 4.5°.

The χ^2 comparison is clearly sensitive to our estimates of azimuthal uncertainties. Systematically overestimated uncertainties will make two sets of observations appear more similar than they really are whereas systematically underestimated uncertainties may lead to the erroneous conclusion that two sets of observations are significantly different. Recalling that we have calibrated the altimetrically-derived uncertainties to be approximately correct, and the geometric technique described in the appendix should give bathymetrically-derived uncertainties that are approximately correct, we conclude that the altimetrically- and bathymetrically-derived transform fault azimuths are not on average significantly different within the $\sim 1°$ precision of the measurements.

4. A qualitative assessment of the altimetrically-derived azimuths

Before undertaking a rigorous assessment of the impact of altimetrically-derived azimuths on esti-

Table 2
Best-fitting rotations

Plate pair	Latitude	Longitude	ω	Error ellipse			σ_ω
Pair	(°N)	(°E)	(deg-m.y.$^{-1}$)	σ_{max}	σ_{min}	ξ_{max}	(deg − m.y.$^{-1}$)
Afr.–Ant. †	0.60	−35.1	0.147	3.2	0.7	−41	0.004
Aust.–Ant. ††	13.0	39.2	0.678	0.7	0.6	−39	0.002
Naz.–Ant.	31.0	−94.9	0.572	3.9	0.5	02	0.014
Pac.–Ant.	−66.7	98.3	0.935	0.8	0.4	−43	0.007
So. Am.–Ant.	64.39	−84.1	0.909	1.2	1.1	66	0.010
Afr.–So. Am.	62.6	−39.6	0.320	1.1	0.3	−12	0.003

† Does not use the two anomalous azimuths at 29.0°E and 31.33°E.

†† Does not use any azimuths east of 147°E.

The first plate moves counterclockwise relative to the second plate. To rescale the angular rotation rate to adjust for a recent recalibration to the young part of the reversal time scale, multiply the angular rotation rate by 0.9562 and the covariances by 0.9562 * * 2 (DeMets et al., 1994b). One sigma-error ellipses are specified by the angular lengths of the principal axes and by the azimuths (ξ_{max}, given in degrees clockwise from north) of the major axis. The rotation rate uncertainty is determined from a one-dimensional marginal distribution, whereas the lengths of the principal axes are determined from a two-dimensional marginal distribution.

Abbreviations: Afr. = Africa; Ant. = Antarctica; Aust. = Australia; Naz. = Nazca; Pac. = Pacific; So. Am. = South America.

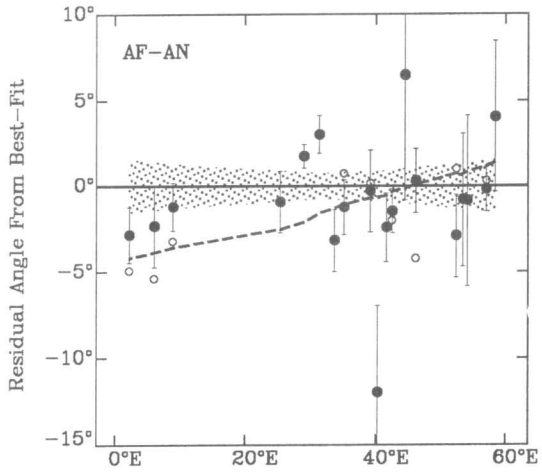
AF–AN
Residual Angle From Best–Fit
10°
5°
0°
−5°
−10°
−15°
0°E
20°E
40°E
60°E

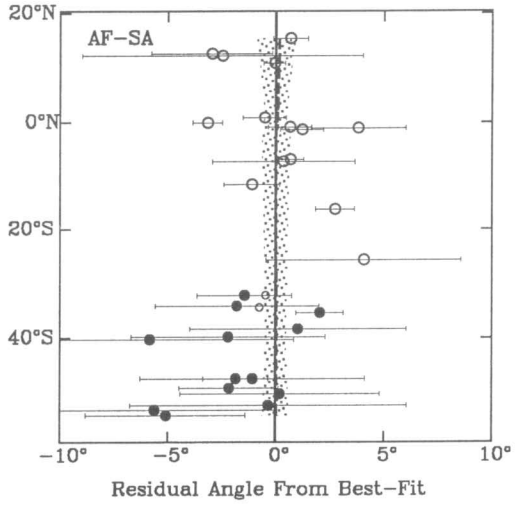
AF–SA
20°N
0°N
20°S
40°S
−10°
−5°
0°
5°
10°
Residual Angle From Best–Fit

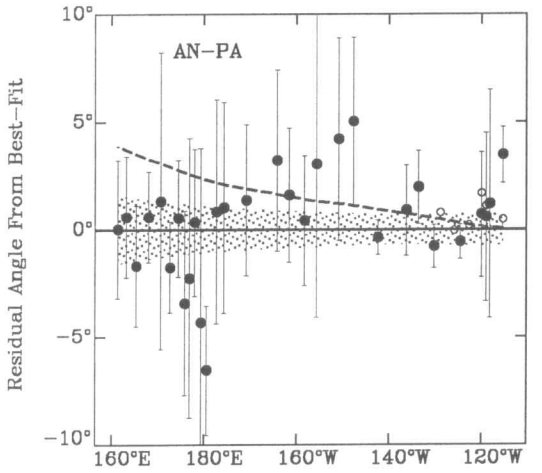
AN–PA
Residual Angle From Best–Fit
10°
5°
0°
−5°
−10°
160°E
180°E
160°W
140°W
120°W

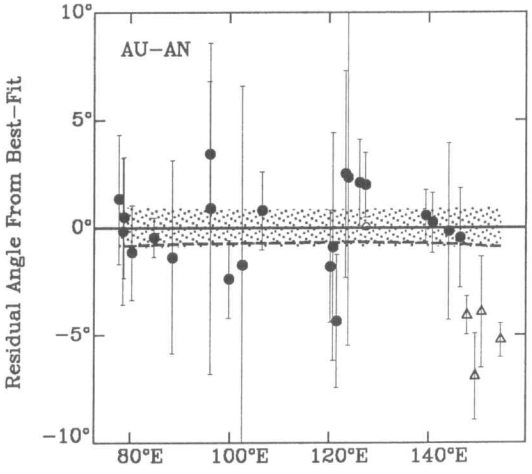
AU–AN
Residual Angle From Best–Fit
10°
5°
0°
−5°
−10°
80°E
100°E
120°E
140°E

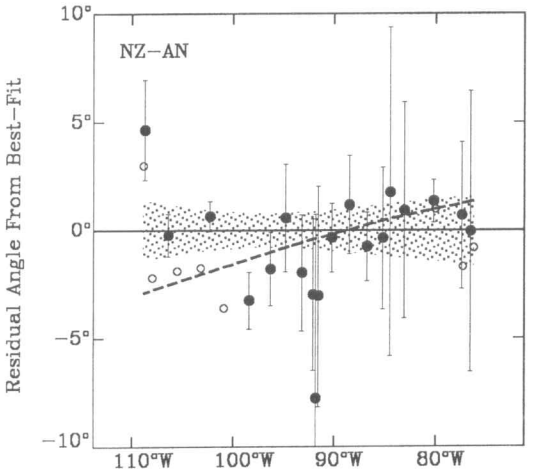
NZ–AN
Residual Angle From Best–Fit
10°
5°
0°
−5°
−10°
110°W
100°W
90°W
80°W

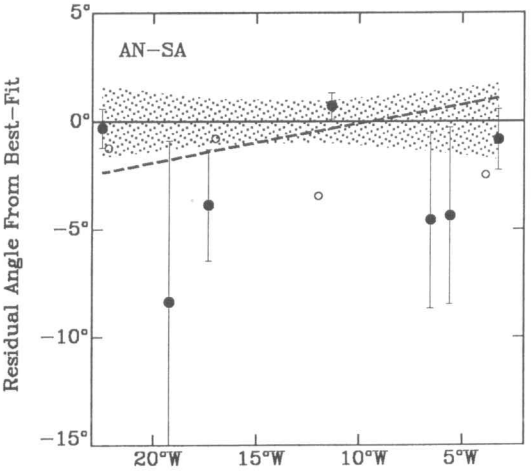
AN–SA
Residual Angle From Best–Fit
5°
0°
−5°
−10°
−15°
20°W
15°W
10°W
5°W

mates of global plate velocities, we first assess how well the new azimuths are fit by the NUVEL-1 angular velocities. Fig. 3 shows the fit for each of the six spreading centers below 30°S. The observed azimuths and NUVEL-1 predictions are shown as residual angles from the predictions of the angular velocities that best-fit the altimetrically-derived azimuths and 3.0-m.y.-average NUVEL-1 spreading rates from these spreading centers. The BFVs and their uncertainties are given in Table 2.

4.1. Africa–Antarctica

Neither the NUVEL-1 Africa–Antarctica angular velocity nor the Africa–Antarctic BFV give a good fit to the 19 altimetrically-derived transform fault azimuths from the slow-spreading Southwest Indian Ridge (Fig. 3). For instance, the BFV has reduced chi-square of 2.0, approximately twice the expected value of 1.0. Two apparently well-constrained, but nonetheless poorly-fit azimuths near 29°E and 31°E (Fig. 3) force a poor fit to the other data. If we invert all Southwest Indian Ridge transform fault azimuths except these two azimuths, reduced chi-square for the remaining 17 transform azimuths decreases to 0.7, roughly one-third the former value.

There are at least two possible explanations for the poor fit to the transform azimuths at 29°E and 31°E. First, the true slip direction along these transform faults could differ from the altimetrically-derived azimuths by several degrees if strike-slip motion within the transform valleys occurs along fault strands that are oblique to the overall transform valley trend. Unfortunately, the prominent gravity signatures of these two long-offset transform faults and the limited 2-D resolution of the altimetric measurements prohibits resolution of features within the transform valleys (Appendix 2, Fig. 7). An upcoming RIDGE cruise that will survey the plate boundary from 15°E to 35°E (Humphris, 1994) should greatly enhance our knowledge of the morphology of this poorly known region.

An alternative explanation for our inability to fit simultaneously all of the observed azimuths with a single rotation axis is the possibility that the African or Antarctic plate is deforming internally. For instance, distributed intraplate seismicity in seafloor south of Africa (Bergman, 1986) may be related to the larger-scale break-up of the African plate indicated by continental scale rifting in eastern Africa. One previous attempt to use kinematic data from the Southwest Indian ridge to detect any rift-related deformation along the Southwest Indian Ridge was unsuccessful (DeMets et al., 1988); however, this might simply indicate that any deformation is so slow that it could not be resolved with the sparse, low-quality data that were previously available. We plan to further examine the present, more complete set of azimuths as part of a larger-scale study of East African rifting (Chu et al., ''Current motion between Nubia and Somalia'', in prep.).

4.2. Africa–South America

The BFV for this plate pair was derived from altimetrically-derived azimuths south of 30°S and newly compiled, bathymetrically-derived estimates for fourteen transform faults as far north as 15°N (see open circles in upper right panel of Fig. 3). North of ~ 40°S, the observed azimuths are relatively evenly scattered about the best-fitting predictions (Fig. 3); however, azimuths located south of ~ 40°S are on average several degrees counterclockwise (CCW) from the best-fitting and NUVEL-1 predictions (note that the NUVEL-1 and best-fitting predictions are nearly indistinguishable in Fig. 3).

Although the several-degree bias of transform fault azimuths south of ~ 40°S could result from

Fig. 3. Altimetrically-derived transform fault azimuths (solid circles) for six spreading centers plotted as residual angles from the directions predicted by best-fitting rotations. Positive residual angles correspond to observations oriented clockwise of predictions. The 95% prediction uncertainties for the best-fitting rotations are shown as stippled regions. Predictions of the NUVEL-1 model (dashed line) are plotted as residuals from the best-fitting directions. Open circles represent bathymetrically-derived azimuths given in Table 1; open circles with error bars represent bathymetrically-derived transform fault azimuths from the Africa–South America plate boundary north of 30°S used to derive the best-fitting rotation; open triangles with error bars represent azimuths of transform faults not used to derive the Australia–Antarctica best-fitting rotation. Abbreviations: *AF* = African plate; *AN* = Antarctic plate; *SA* = South American plate; *PA* = Pacific plate; *AU* = Australian plate; *NZ* = Nazca plate.

random or small systematic errors within this small sample, slow distributed deformation of the South American plate east of the South Sandwich trench might also explain the bias. An enhanced level of intraplate seismicity in this region (Bergman, 1986) is apparent in our compilation of post-1963 earthquake epicenters and Harvard centroid-moment tensor solutions for post-1976 earthquakes in the southern Atlantic (Fig. 4). The region of scattered off-ridge seismicity west of the Mid-Atlantic Ridge and south of ~ 47°S is characterized by strike-slip motion that parallels either the NE- or SE-trending nodal planes (Fig. 4).

One plausible, though speculative model for this deformation is that the off-ridge strike-slip earthquakes accommodate dextral slip along NE-trending

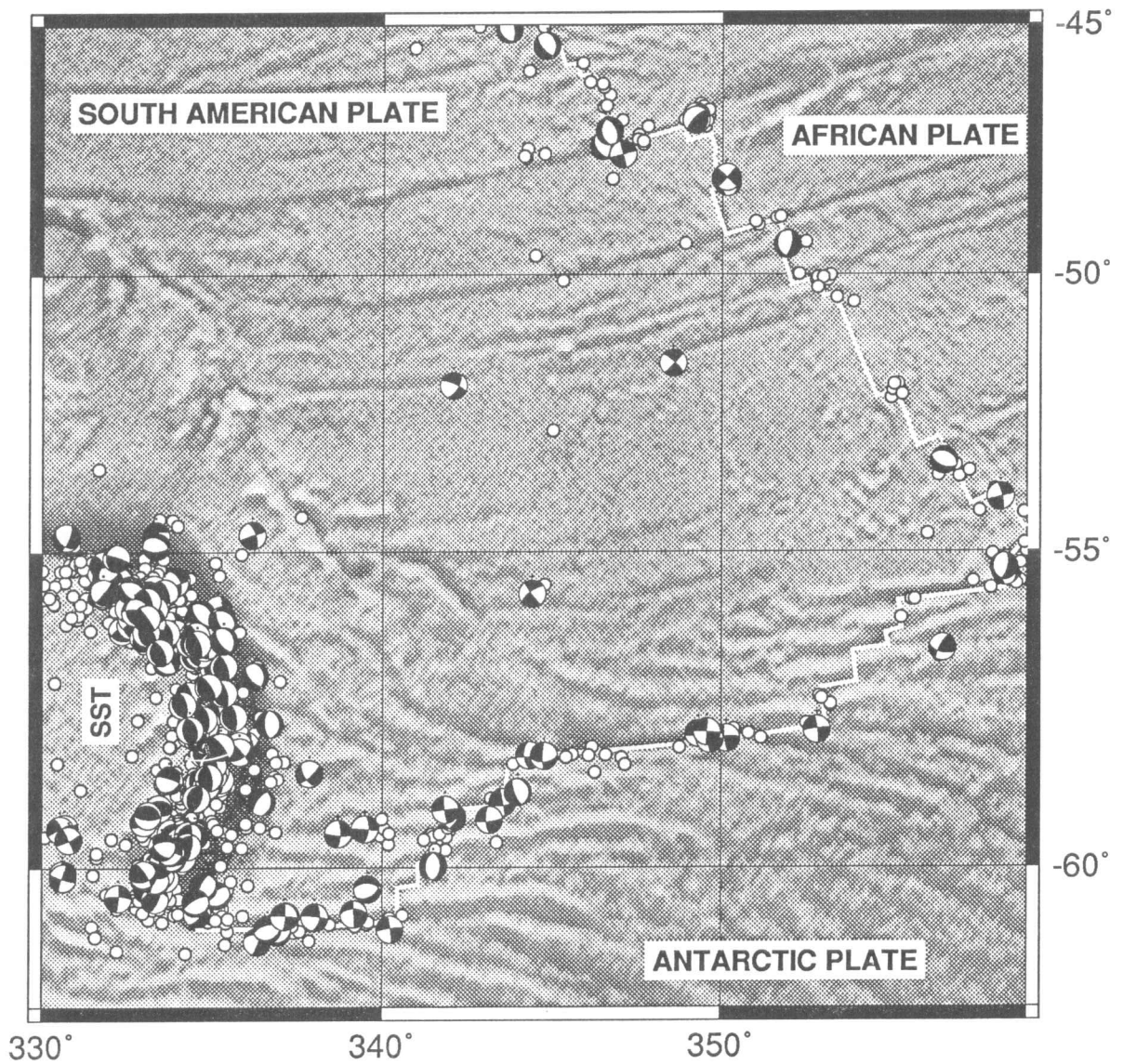

Fig. 4. Free-air gravity anomalies, post-1963 earthquake epicenters, and post-1976 earthquake focal mechanisms derived from Harvard centroid-moment tensor solutions in the southern Atlantic. All epicenters and focal mechanisms are for earthquakes shallower than 60 km depth. *SST* = South Sandwich Trench.

faults, in which case seafloor south of ~ 47°S and west of the Mid-Atlantic Ridge moves to the southwest relative to South American lithosphere farther north. Seafloor west of the ridge and south of ~ 47°S must then move more CCW relative to the African plate than stable South American lithosphere north of the deforming zone. Transform faults offsetting the Mid-Atlantic ridge south of 47°S could accommodate this additional southerly component by developing a "leaky" component or by realigning themselves in a direction parallel to the more CCW slip direction. The previously mentioned CCW bias of transform faults south of 40°S favors the latter mechanism (Fig. 3).

Westward subduction of oceanic lithosphere located east of the South Sandwich trench might explain why lithosphere east and northeast of the trench moves more quickly westward than South American lithosphere farther north. This speculative model also predicts that spreading rates along the southern Mid-Atlantic ridge are faster than predicted by the NUVEL-1 Africa–South America angular velocity; however, spreading rates from this region are too poorly known to test this prediction.

4.3. Antarctic–Pacific

The 30 newly-derived azimuths transform fault azimuths from the Pacific–Antarctic rise are fit well by the BFV, with no evidence for systematic misfits (Fig. 3). The BFV predicts motion systematically CCW from that predicted by NUVEL-1, with a maximum observed difference of 4°, approximately twice the ±2° 95% prediction uncertainty of the NUVEL-1 angular velocity (Fig. 3). The many new azimuths thus provide significant new information regarding motion between these two plates. In a separate study, we will discuss how estimates of Pacific–Australia velocities along the long boundary between these two plates are affected by the new Pacific–Antarctic and Australia–Antarctic transform fault azimuths when closure of the Pacific–Antarctic–Australia plate circuit is required.

4.4. Australia–Antarctic

The twenty-six altimetrically-derived transform fault azimuths from this spreading center show a pattern similar to that found by DeMets et al. (1988), namely, that slip directions east of ~ 145°E are rotated significantly CCW from the directions predicted by the Australia–Antarctic BFV (Fig. 3). In particular, the four transform fault azimuths east of 147°E force a poor overall fit to the 26 transform fault azimuths, with reduced chi-square of 2.3. If we reinvert Australia–Antarctic data while excluding the four poorly-fit azimuths east of 147°E, reduced chi-square for the remaining 22 azimuths decreases to only 0.5, indicating that this subset of the Southeast Indian Ridge transform azimuths is well fit by a single angular velocity. The likelihood that random errors in the four poorly-fit azimuths are responsible for the observed poor fit to the remaining 22 azimuths is less than 0.01%.

The nearly five-fold increase in misfit that occurs if the four easternmost transform azimuths are assumed to parallel Australia–Antarctic motion has either a tectonic origin or indicates a problem in the azimuths we have estimated. We cannot exclude the possibility that the estimated azimuths are biased by the presence of multiple, obliquely-oriented fault strands within these long-offset transform valleys; however, for reasons outlined below, we favor an explanation proposed by DeMets et al. (1988), namely, that the Australian plate west of the Macquarie triple junction is deforming. First, the free-air gravity signatures and gradients of these four transforms are reasonably well defined (Appendix 9, Fig. 14). We experimented with a variety of interpretations of the plate boundary configuration east of 147°E and had difficulty finding any interpretation that yielded transform azimuths more than ±1.5° different from those given in Table 1. Second, slip directions from numerous strike-slip earthquakes along the four transform faults are also rotated several degrees CCW from the predicted Australia–Antarctic direction (DeMets et al., 1988), even after correction for a systematic bias in transform fault slip directions (DeMets, 1993). Finally, significant seismicity within the Australian plate west of the Macquarie Ridge Complex and gravity undulations that might indicate buckling of seafloor in the same region (Stewart, 1983; Valenzuela and Wysession, 1993) suggest that the Australian plate west of the Macquarie Ridge Complex may experience slow and possibly distributed deformation, possibly in re-

sponse to westward overriding of the Pacific plate along the Macquarie Ridge Complex. We plan to treat this topic in greater depth in a related manuscript concerning the kinematics of this region and implications for motion between the Pacific and Australian plates.

4.5. Nazca–Antarctic

Azimuths from this plate boundary cluster into two groups, one consisting of the 16 transform azimuths east of 100°W, and the other consisting of three azimuths from the long and nearly continuous Chile transform fault west of 100°W (Fig. 3 and Appendices 15 and 16, Figgs. 20 and 21). The NUVEL-1 Nazca–Antarctic angular velocity fits the 16 azimuths located east of 100°W, but misfits the three west of 100°W. Both the NUVEL-1 model and westward-extrapolated trend defined by the 16 azimuths east of 100°W suggest that the true slip directions west of 100°W are several degrees CCW from the directions we have interpreted from the free-air gravity anomalies.

This raises the question of whether the three altimetrically-derived azimuths from the Chile transform fault west of 100°W reliably describe the present slip direction. Independent evidence suggests they do not. Bathymetric and side-scan sonar images of the Chile transform west of 107°W show that strike-slip motion within the transform valley is accommodated by a series of westerly-trending faults connected by extensional relay zones (see fig. 2 in Larson et al. (1992) and figs. 6 and 8a in Kleinrock and Bird (1994)). As shown in Fig. 3, the westerly-trending faults strike several degrees CCW from the azimuth of the transform valley, but agree well with the directions predicted by both NUVEL-1 and the altimetrically-derived azimuths from east of 100°W.

The several degree difference between the altimetrically-derived and the more reliable bathymetrically-derived transform fault azimuths along the western Chile Rise illustrates an important unavoidable shortcoming of the use of altimetry for determining transform fault azimuths — the limited spatial resolution prevents imaging of strike-slip features within the transform valley. If multiple fault strands oriented oblique to the overall trend of the valley exist, as is the case along the western Chile transform fault, altimetrically-derived azimuths will misstate the true slip direction.

4.6. Antarctic–South America

The pattern of transform slip directions along the American–Antarctic rise is principally defined by the long-offset Conrad (3°W), Bullard (12°W), and South Sandwich (22°W) transform faults (Fig. 3 and Appendix 16, Fig. 21). To our knowledge, none of these faults have been mapped with a modern swath-mapping system; however, the azimuths of the Conrad and Bullard transform faults, which offset the ridge by 190 km and 530 km respectively, are well-constrained by altimetry and suggest that the directions predicted by NUVEL-1 are accurate to within $\pm 3°$ along this spreading center.

4.7. Summary of NUVEL-1 Fit

Fig. 5 summarizes the weighted angular differences between the 110 altimetrically-derived az-

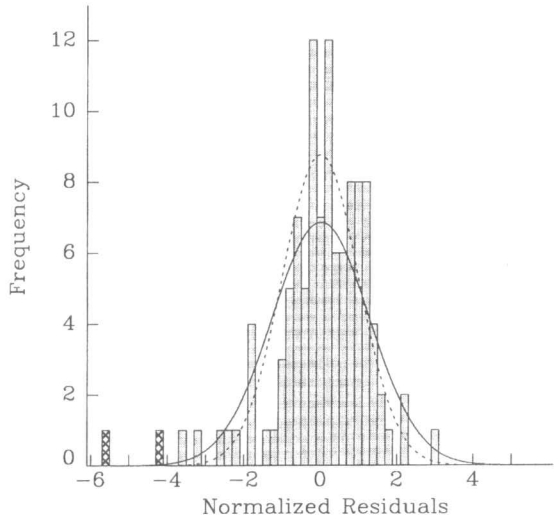

Fig. 5. Histogram of weighted angular differences between the altimetrically-derived azimuths and those predicted by NUVEL-1 for the 110 transform faults analyzed here. Solid line shows a Gaussian distribution with a mean of zero and standard deviation of 1; dashed line shows the Gaussian distribution for the mean and standard error computed from the observed distribution of residuals. The normalized residuals are computed by dividing the difference between the predicted and observed azimuths by the data uncertainty. The two outliers with a cross-hatched pattern are the Africa–Antarctic transforms located at 29.0°E and 31.33°E.

imuths and directions predicted by NUVEL-1. Each residual angle has been divided by the uncertainty assigned to the altimetrically-derived azimuth, but not by the prediction uncertainty since these uncertainties are highly correlated for any given plate boundary. The distribution of weighted residual angles is approximately Gaussian with a weighted mean misfit of $-0.5°$ and a standard error of the mean of $\pm 0.2°$. Although the weighted mean misfit is significantly different from zero, its value is strongly affected by the two poorly fit transform azimuths at 29°E and 31°E along the Southwest Indian Ridge, which appear as large negative outliers (-4.2 and -5.5 sigma). If we exclude these two outliers, the weighted mean misfit reduces to only $-0.2° \pm 0.4°$ (95%).

5. Implications for estimates of global plate velocities

The preceding analysis suggests that the altimetrically-derived azimuths contain significant new information regarding plate velocities between the Pacific and Antarctic plates, and African and Antarctic plates; however, a rigorous determination of the effect of the altimetrically-derived azimuths requires comparison of a plate motion model derived using the newly available azimuths to one, such as NUVEL-1, that does not. Below, we undertake such a comparison, focusing on how two alternative plate motion models derived using the altimetrically-based azimuths given in Table 1 fit plate motion data relative to a model like NUVEL-1.

5.1. Construction of plate motion models

We first derived two trial models of global plate motions, one (Model N) using a subset of the 1122 NUVEL-1 data, but no altimetrically-derived azimuths, and the other (Model A) using these same data, but substituting the 110 altimetrically-derived azimuths for the NUVEL-1 transform azimuths below 30°S. In total, 1015 of the original 1122 NUVEL-1 data are used to derive Model N. Model A is derived from 1071 data, of which 961 are taken from the 1015 NUVEL-1 data described above, and 110 are altimetrically-derived transform azimuths that replace all NUVEL-1 transform fault azimuths located south of 30°S.

We did not use NUVEL-1 for the comparison for several reasons. First, the NUVEL-1 data uncertainties are not assigned in a manner consistent with that used to assign uncertainties to the altimetrically-derived azimuths, resulting in NUVEL-1 covariances that are significantly larger than required by the data. To correct for this, we multiplied the NUVEL-1 rate, transform, and slip vector uncertainties by factors of 0.438, 0.577 and 0.494 to achieve a reduced chi-square of 1.0 for each of these data subsets. These scaling factors were determined through examination of the chi-square misfits and cumulative data importances for subsets of the NUVEL-1 data (DeMets et al., 1990). Second, for Model N, we chose to adopt a geometry for the Australian plate in which the rigid part of the Australian plate north of the Southeast Indian Ridge does not extend east of 147°E. This differs from the geometry adopted in NUVEL-1. To accomplish this, we omitted the thirty-nine NUVEL-1 data from the four easternmost transform faults along the Southeast Indian Ridge. Finally, we also had to omit all kinematic data from the boundaries of the Arabian and Indian plates because neither of these plates had a direct or indirect link through plate circuit closures to the plate boundaries relevant to this analysis.

We inverted each of the data sets described above to derive a set of angular velocities that minimize the cumulative least-squares misfits to the respective data sets while simultaneously satisfying the requirement of closure within the many sub-circuits that comprise a global plate circuit. The angular velocities that comprise Model N and NUVEL-1 are nearly identical (as expected), with only minor differences (± 0.1 mm yr^{-1} and $\pm 0.1°$) in predicted velocities along most plate boundaries. The small differences between the Model N and NUVEL-1 angular velocities result from the fact that the uncertainties assigned to the rates, transforms, and slip vectors are weighted in a manner slightly different than in the original NUVEL-1 study, and from the omission of the 45 kinematic data along the eastern Australia–Antarctic plate boundary.

Values of χ_v^2 for Models N and A are 1.02 and 1.07, respectively, indicating that the data uncertainties are correctly calibrated. Each model includes 10

plates, of which one is fixed to establish a reference frame. The angular velocities of the remaining nine plates are completely described by 27 adjustable parameters, corresponding to a latitude, longitude, and angular rotation rate for each of the nine angular velocities. The weighted misfits and data importances of all of the input data were also computed following the inversion, enabling us to compare easily the fits of both models to various subsets of the data.

5.2. Comparison of Models A and N

The easiest way to ascertain whether the altimetrically-derived azimuths force significant changes in the angular velocities that describe present-day plate motions is to compare the fits of Models A and N to different subsets of the kinematic data. For instance, to determine whether Model N provides an adequate fit to the altimetrically-derived azimuths, the fits of Models N and A to the 110 altimetrically-derived azimuths must be compared. A significant difference in the fits of Models A and N would indicate that relative to Model N, significant adjustments in the Model A angular velocities were required in order to fit the altimetrically-derived azimuths. Similarly, a comparison of the fits of Model A and Model N to spreading rates and other kinematic data located north of 30°S establishes whether or not incorporation of the altimetrically-derived azimuths into a global kinematic data set forces significant misfits to other kinematic data.

To compare the fits of alternative models, we use the F-ratio test, where:

$$F_{(m_1-m_2,N-m_1)} = \frac{\left[\chi^2(m_2) - \chi^2(m_1)\right]/(m_1 - m_2)}{\chi^2(m_1)/(N - m_1)} \quad (2)$$

$\chi^2(m_1)$ is the least-squares misfit of Model 1 to the N observations, and m_1 represents the number of model parameters adjusted in Model 1 to fit these N observations. Similarly, $\chi^2(m_2)$ is the least-squares misfit of Model 2, and m_2 represents the number of model parameters adjusted in Model 2 to fit these same N observations. The number of model parameters constrained by a given number of data is determined by summing their data importances (Minster et al., 1974).

5.3. Fits of Models A and N to the altimetrically-derived azimuths

For the 110 altimetrically-derived azimuths, $\chi^2(m_N) = 181.4$ and $\chi^2(m_A) = 137.0$. In Model N, no parameters were adjusted to improve the fit to these data; in Model A, 4.6 out of 27 angular velocity components were constrained by the 110 azimuths (the remaining 22.4 parameters were constrained by the other 961 data). Applying (2) gives $F = 7.4$. For comparison, the threshold value for F at the 99% confidence level is 3.3. The angular velocities that comprise Model A thus fit the 110 azimuths significantly better than those of Model N.

5.4. Fits of Models A and N to the remaining data

For the 961 kinematic data other than the altimetrically-derived azimuths, including all spreading rates and earthquake slip vectors north and south of 30°S, and all transform fault azimuths north of 30°S, the least-squares misfits of Model N and Model A are $\chi^2(m_N) = 973.6$ and $\chi^2(m_A) = 982.6$, respectively. The 961 observations constrain 24.87 of 27 model parameters in Model N and 22.42 of 27 model parameters in Model A. Applying (2) gives $F = 3.5$, indicating that the fits differ at the 98% confidence level. Even if this result is reliable (which we doubt for reasons described below), the maximum differences in the velocities predicted by these two models are small, ~ 0.3 mm yr^{-1} and 1.7°.

5.5. Results upon exclusion of two anomalous azimuths

To determine how the two previously mentioned anomalous azimuths from the Southwest Indian Ridge influenced Model A and the fit of Model A to the data described above, we eliminated these two azimuths from the data used to derive Model A and derived a new model (Model A') from the remaining data. We then repeated the comparison of the model fits to the altimetrically-derived and other kinematic data. Model N and Model A' give respective fits to the remaining 108 altimetrically-derived azimuths of

$\chi^2(m_N) = 128.4$ and $\chi^2(m_{A'}) = 100.7$. The 108 azimuths constrain 4.5 adjustable parameters in Model A'. Applying (2) gives $F = 6.3$, well above the 99% confidence level for a significant difference between the two fits. Thus, even without the two azimuths, Model A' provides a significantly better fit than Model N.

For the remaining 961 data, the fit of Model N remains the same as above [$\chi^2(m_N) = 973.6$], but the fit of Model A' improves significantly to $\chi^2(m_{A'}) = 974.2$, only slightly higher than that of Model N. For the 22.5 degrees of freedom constrained in Model A' by the 961 data, Eq. 2 gives $F = 0.25$, indicating that the fits of the two models are nearly identical. Thus, the two poorly-fit altimetrically-derived azimuths from the Southwest Indian Ridge are responsible for much of the the previously mentioned significant difference between the fits of Models N and A to the remaining 961 kinematic data.

6. Discussion and summary

Several useful conclusions can be drawn from the results described above. First, the good agreement between transform fault azimuths derived from altimetric observations and those determined using ship-board observations suggests that altimetrically-derived transform fault azimuths can be used to represent present-day slip directions in regions that lack reliable bathymetrically-derived azimuths. However, along the western Chile transform fault, altimetrically-derived azimuths are demonstrably biased relative to the slip direction defined by higher-resolution ship-board observations, suggesting that caution must be exercised when interpreting misfits to geographically isolated transform fault azimuths; misfits to azimuths from several nearby transform faults are more likely to be significant.

Our comparison of global plate motion models derived with and without the benefit of the altimetrically-derived azimuths indicates that the models derived from data sets that include the altimetrically-derived azimuths fit these azimuths significantly better than a model derived without the azimuths. Moreover, the use of the altimetrically-derived azimuths within a closure-enforced global plate motion model causes only a small increase in the misfit to other data such as spreading rates and earthquake slip vectors. Thus, the altimetrically-derived azimuths offer two important benefits — they provide significant new information about present-day plate velocities, particularly along the Africa–Antarctic and Pacific–Antarctic plate boundaries, without significantly altering the already good fit of the NUVEL-1 model to globally-distributed kinematic data.

The 108 altimetrically-derived azimuths used to derive Model A' also offer two additional benefits. First, they constrain 4.5 of the 27 adjustable parameters in Model A', approximately twice the 2.1 adjustable parameters constrained in Model N by the NUVEL-1 transform azimuths from below 30°S. The altimetrically-derived azimuths thus improve the balance of kinematic information provided by data south of 30°S, where nearly 40% of the mid-ocean ridge system is located. The new azimuths also reduce by ~ 10% the Model A' covariances relative to those of Model N. The decreased covariances, which result from the improved geographic distribution of the azimuths as well as the increase in their numbers, are useful in part because they permit stronger tests of plate circuit closure useful for detecting regions of intraplate deformation.

Acknowledgements

We thank Graham Westbrook for providing unpublished azimuths of transform faults from the eastern Chile Rise and J.G. Schilling for providing unpublished azimuths of transform faults from the equatorial Atlantic. We also thank Philippe Patriat and Dave Sandwell for constructive reviews. This work was supported by NSF Grant EAR-9205083 and George Woollard funds.

Appendix A. Estimating transform fault locations and azimuths

The gridded free-air gravity data were displayed in three different ways using Generic Mapping Tool software developed by Wessel and Smith (1991). We plotted simple gray-scale images of the gridded data at a scale large enough (0.5–1.0 inch per degree of

longitude) to see details of the ridge-transform configuration. To enhance the prominent gravitational gradients often associated with transform valleys and axial valleys, we also solved for and displayed in color the gravitational gradient in two directions, one parallel and the other orthogonal to that predicted by NUVEL-1.

Using the large-scale maps described above, we carefully traced the ridge segments and their offsets for each spreading center, trying to avoid awkward and probably implausible ridge-transform configurations such as sudden reversals in the sense of oblique spreading along a spreading center. We interpreted transform fault trends and locations as parallel to and as close to the center of the linear gravity low associated with transform fault valleys as was possible. We then digitized our interpreted plate boundaries and compared them to our original traces to ensure that no errors had been introduced. Finally, we computed the geographic mid-point of each transform fault, its azimuth, and an angular uncertainty for the azimuth (described below). All azimuths were rounded to the nearest 0.5°, reflecting the level of uncertainty introduced by the digitization (also described below).

Appendices 1–19 (Figs. 6–24) show the marine free-air gravity field and its transform-orthogonal gradient for the entire mid-ocean ridge system south of 30°S. We chose to show the transform-normal gradient because it serves to emphasize the prominent slopes associated with transform valleys and fracture zones. The ridge-normal gradient, though not shown to save space, was useful for identifying the locations of spreading segments.

Estimating transform fault azimuthal uncertainties. There are three sources of uncertainty in the azimuths we estimate, namely, a geometrically-defined uncertainty related to the location and orientation of the active fault within a transform valley, and a small random uncertainty introduced during the process of digitizing the plate boundary, and a possible uncertainty related to the seafloor age-offset of a transform fault.

Geometrically-related uncertainties. The first source of uncertainty is related to our ignorance of the true orientation of the active fault strand or strands that are located within a transform valley that is approximately rectangular in plan view (Garfunkel, 1986). Lacking high-resolution bathymetric or side-scan sonar data that define the arrangement of active faults within a transform valley, we assume that the plate slip direction parallels the overall trend of the valley and has an uncertainty α that depends on the length and width of the transform valley. Long, narrow valleys strongly constrain the range of permitted fault azimuths within them whereas short, wide valleys have a wide range of geometrically-constrained azimuths. Simple geometry can be used to demonstrate that the geometrically-defined angular uncertainty α is the inverse tangent of the transform width divided by its length, as suggested by R.G. Gordon and briefly described in DeMets et al. (1994a).

To determine the standard deviation of the best estimate for an azimuth, a probability distribution for the range of possible azimuths must be assumed. We chose to assume that the probability of observing any particular azimuth within the geometrically permitted range is equal. Since the total permitted angular deviation on each side of the best estimate is $\alpha°$, the probability of observing any given azimuth is $1/(2\alpha)$. Using Eq. 1.14 in Bevington and Robinson (1992) to derive the variance σ^2, the 1σ uncertainty is then found to be $\alpha/\sqrt{3}$.. Adoption of a Gaussian probability distribution would yield somewhat smaller 1σ uncertainties, although one cannot state exactly how much smaller without first specifying whether α corresponds to a 95%, 99%, or other limit on the range of geometrically-permitted azimuths.

Digitizing the interpreted fault locations introduces a small additional uncertainty into the estimated azimuths. Through repeated digitization of the same feature on our digitizing table, we found that the sample standard deviation from the computed mean azimuth was $\pm 0.36°$, considerably smaller than the smallest geometrically-defined uncertainty of $\pm 0.6°$. To account for this uncertainty, we rounded all azimuths to the nearest 0.5° and computed the overall azimuthal uncertainty by summing in quadrature the geometrically-defined and digitization uncertainties.

Uncertainties related to the age-offset of a transform. An additional, potentially important source of uncertainty in transform fault azimuths is that gravity signatures of transform faults with seafloor age-offsets of more than several million years might not

accurately record present-day plate slip directions because their present morphology results from plate-boundary slip over a period equal to the age offset of the transform fault, which in some instances can be more than 50 Myr. To investigate this, we first assessed whether there are systematic differences between azimuths derived from large and small age-offset transform faults, and we then examined whether the uncertainties assigned to azimuths of large age-offset transform faults might be too small relative to uncertainties assigned to the small age-offset transform fault azimuths. The latter issue is of concern because of the possibility that an azimuthal uncertainty might depend not only on the width and length of the transform valley (as is described elsewhere in this paper), but also on the magnitude of its age offset. Here, "large" and "small" age-offset refer to transform faults with age offsets that are greater than and less than ~ 5 Myr, respectively.

To treat the question of the reliability of large age-offset transform faults for approximating present-day slip directions, we posed the following question: If large age-offset transform faults do not on average parallel present-day slip directions, then best-fitting angular velocities derived solely from the azimuths of large age-offset transform faults should differ significantly from those derived solely from azimuths of small age-offset transforms. Statistically, this question can be answered by determining whether the least-squares misfit of an angular velocity that best-fits all transform fault azimuths (large age-offset and small age-offset) from a given plate boundary differs significantly from the summed least-squares misfits of two best-fitting angular velocities, one of which best-fits only the large age-offset transforms and the other of which best-fits only the small age-offset transforms. An F-ratio test is used to compare the fits of these models.

For all of the transform faults in Table 1, we computed the maximum seafloor age contrast across the transform valley by dividing the transform length by the full spreading rate estimated from the NUVEL-1A model. As stated above, small and large age-offset transforms were defined as having age offsets less than or greater than 5 m.y., respectively; however, for two of the six spreading centers considered here (Antarctic–South America and Africa–Antarctica), we used 10 m.y. as the dividing point because almost no transform faults had age offsets less than 5 m.y.

For each spreading center, we separately inverted the small age-offset, large age-offset, and combined sets of azimuths to find their respective best-fitting angular velocities and associated least-squares misfits (χ^2). F was computed as follows:

$$F_{(2,N-4)} = \frac{\left[\chi^2_{\text{all}} - \left(\chi^2_{\text{large}} + \chi^2_{\text{small}}\right)\right]/2}{\left(\chi^2_{\text{large}} + \chi^2_{\text{small}}\right)/(N-4)} \qquad \text{(A.1)}$$

where χ^2_{all} is the least-squares misfit to all of the transform azimuths when inverted simultaneously, and χ^2_{large}, and χ^2_{small} are the misfits to the large and small age-offset transform azimuths, respectively. N represents the total number of transform fault azimuths, and "2" represents the difference in the degrees of freedom required to fit one set of azimuths as opposed to fitting two sets of azimuths (i.e. only one rotation axis is required instead of two rotation axes). Employed in this manner, the F-ratio test permits us to determine whether the large and small age-offset azimuths are mutually consistent within their assigned uncertainties.

Of the six spreading centers south of 30°S, none show differences between the large and small age-offset transform azimuths that are significant at the 95% confidence level. Thus, within the assigned uncertainties, there is no evidence that the two subsets of azimuths provide significantly different descriptions of present-day slip directions. The only notable systematic difference is a small $\sim 1°$ CW rotation of five large age-offset transform azimuths along the Pacific-Antarctic rise relative to azimuths predicted by a rotation axis derived solely from small age-offset transforms; however, this small difference is not statistically significant.

Finally, we also examined whether our simple scheme for assigning azimuthal uncertainties based primarily on transform fault lengths and widths could have inadvertently led to uncertainties for the large age-offset transforms that are too small relative to those assigned to small age-offset transforms. In any large data population whose residuals follow a χ^2 distribution, random subsets of the data population should show approximately the same scatter relative to the predictions of some underlying model (such as a best-fitting angular velocity) if the assumptions

used to assign the data uncertainties are correct (or nearly so). If we are correct in our assumption that the age offset of a transform fault is not an important factor in assigning uncertainties, the dispersions of the small and large age-offset transform fault azimuths relative to their best-fitting rotations should be similar.

For each spreading center, we separately inverted the large and small age-offset transform fault azimuths, and tabulated the cumulative least-squares misfits and data importances. For the 73 small age-offset transforms, the cumulative chi-square is 40.0 with a total data importance of 7.47. For the 37 large age-offset transforms, the cumulative chi-square is 48.4 with a total data importance of 8.75. Reduced chi-square is thus 0.60 and 1.71 for the small and large age-offset transforms. If we exclude the two poorly fit large age-offset transforms along the Africa–Antarctic plate boundary (at 29.0°E and 31.33°E), reduced chi-square for the latter decreases to 0.95. The large age-offset transform azimuths thus have a larger inherent dispersion than the small age-offset azimuths, but the majority of the difference stems from only two of the 37 large age-offset transforms. Application of a simple F-ratio test to compare values of reduced chi-square shows that the two values of reduced chi-square do not differ at the 99% confidence level unless the two outliers along the Africa–Antarctic plate boundary are included.

Problems associated with large age-offset transform faults and their uncertainties are thus primarily isolated to two out of the fourteen large age-offset transform faults along the Southwest Indian ridge; the remaining 35 large age-offset transform faults have azimuths and uncertainties that are consistent with those estimated for small age-offset transforms. This suggests that our interpretation of the complex altimetric signatures of these two anomalous transform faults may be in error by several degrees. In the ensuing analysis, we thus prefer to treat these two anomalous azimuths as special cases rather than to implement an azimuthal weighting scheme that not only accounts for the geometry of the transform valley, but also downweights transform azimuths once their age-offset exceeds some pre-defined limit.(Figs. 6–16, 1, 17–21, 6422625, 6553699, 6684773, 102, 22–24)

References

Anderson-Fontana, S., Engeln, J.F., Lundgren, P., Larson, R.L. and Stein, S., 1987. Tectonics of the Nazca–Antarctica plate boundary. Earth Planet. Sci. Lett., 86: 46–56.

Barker, P.F. and Lawver, L.A., 1988. South American–Antarctic plate motion over the past 50 Myr, and the evolution of the South American–Antarctic ridge. Geophys. J.R. Astron. Soc., 94: 377–386.

Bergman, E.A., 1986. Intraplate earthquakes and the state of stress in oceanic lithosphere. Tectonophysics, 132: 1–35.

Bevington, P.R. and Robinson, D.K., 1992. Data Reduction and Error Analysis for the Physical Sciences. New York, McGraw-Hill, Inc.

DeMets, C., Gordon, R.G. and Argus, D.F., 1988. Intraplate deformation and closure of the Australia-Antarctica–Africa plate circuit. J. Geophys. Res., 93: 11,877–11,897.

DeMets, C., Gordon, R.G., Argus, D.F. and Stein, S., 1990. Current plate motions. Geophys. J. Int., 101: 425–478.

DeMets, C., 1993. Earthquake slip vectors and estimates of present-day plate motions. J. Geophys. Res., 98: 6703–6714.

DeMets, C., Gordon, R.G. and Vogt, P., 1994a. Location of the Africa–Australia–India triple junction and motion between the Australian and Indian plates: Results from an aeromagnetic investigation of the Central Indian and Carlsberg ridges. Geophys. J. Int., 119: 893–930.

DeMets, C., Gordon, R.G., Argus, D.F. and Stein, S., 1994b. Effect of recent revisions to the geomagnetic reversal timescale on estimates of current plate motions. Geophys. Res. Lett., 21: 2191–2194.

Dick, H.J.B., Schouten, H., Meyer, P.S., Gallo, D.G., Bergh, H., Tyce, R., Patriat, P., Johnson, K.T.M., Snow, J. and Fisher, A., 1991. Tectonic evolution of the Atlantis II Fracture Zone. In: R.P. Von Herzen, P.T. Robinson et al. (Editors), Proceedings of the Ocean Drilling Program, Scientific Results, 118: 359–398.

Fisher, R.L. and Sclater, J.G., 1983. Tectonic evolution of the Southwest Indian Ocean since the Mid-Cretaceous: Plate motions and stability of the pole of Antarctica/Africa for at least 80 Myr. Geophys. J.R. Astron. Soc., 73: 553–576.

Fox, P.J. and Gallo, D.G., 1989. Transforms of the eastern central Pacific. In: E.L. Winterer, D.M. Hussong and R.W. Decker (Editors), The Eastern Pacific Ocean and Hawaii, The Geology of North America Volume N. Geol. Soc. Am., Boulder, CO, pp. 111–124.

Fox, P.J., Grindlay, N.R. and Macdonald, K.C., 1991. The Mid-Atlantic Ridge (31°S–34° 30'S): Temporal and spatial variations of accretionary processes. Mar. Geophys. Res., 13: 1–20.

Gahagan, L.M., Scotese, C.R., Royer, J.-Y., Sandwell, D.T., Winn, J.K., Tomlins, R.L., Ross, M.I., Newman, J.S., Muller, R.D., Mayes, C.L., Lawver, L.A. and Heubeck, C.E., 1988. Tectonic fabric map of the ocean basins from satellite altimetry data. Tectonophysics, 155: 1–26.

Garfunkel, Z., 1986. Review of oceanic transform activity and development. J. Geol. Soc. London, 143: 775–784.

Grindlay, N.R., Fox, P.J. and Macdonald, K.C., 1991. Second-

order ridge axis discontinuities in the south Atlantic: Morphology, structure, and evolution. Mar. Geophys. Res., 13: 21–50.

Jestin, F., Huchon, P. and Gaulier, J.M., 1994. The Somalia plate and the East African Rift System: Present-day kinematics. Geophys. J. Int., 116: 637–654.

Hartnady, C.J., 1990. Seismicity and plate boundary evolution in southeastern Africa. S. Afr. J. Geol., 93: 473–484.

Humphris, S.E., 1994. Current research sites of the RIDGE initiative. RIDGE events, 5: 16.

Kleinrock, M.C. and Bird, R.T., 1994. Southeastern boundary of the Juan Fernandez microplate: braking microplate rotation and deforming the Antarctic plate. J. Geophys. Res., 99: 9237–9261.

Kuo, B.Y., 1993. Thermal anomalies beneath the Australian–Antarctic discordance. Earth Planet. Sci. Lett., 119: 349–364.

Larson, R.L., Searle, R.C., Kleinrock, M.C., Schouten, H., Bird, R.T., Naar, D.F., Rusby, R.I., Hooft, E.E. and Lasthiotakis, H., 1992. Roller-bearing tectonic evolution of the Juan Fernandez microplate. Nature, 356: 571–576.

le Roex, A.P., Dick, H.J.B., Reid, A.M. and Erlank, A.J., 1982. Ferrobasalts from the Spiess Ridge segment of the Southwest Indian Ridge. Earth Planet. Sci. Lett., 60: 437–451.

Lonsdale, P., 1986. Tectonic and magmatic ridges in the Eltanin fault system, South Pacific. Mar. Geophys. Res., 8: 203–242.

Lonsdale, P., 1994. Geomorphology and structural segmentation of the crest of the southern (Pacific–Antarctic) East Pacific Rise. J. Geophys. Res., 99: 4683–4702.

Marks, K.M., Vogt, P.R. and Hall, S.A., 1990. Residual depth anomalies and the origin of the Australian–Antarctic discordance. J. Geophys. Res., 95: 17,324–17,337.

Marks, K.M., McAdoo, D.C. and Smith, W.H.F., 1993. Mapping the Southwest Indian Ridge with Geosat. Eos Trans. AGU, 74: 81–86.

Mayes, C.L., Lawver, L.A. and Sandwell, D.T., 1990. Tectonic history and new isochron chart of the South Pacific. J. Geophys. Res., 95: 8543–8567.

Minster, J.B. and Jordan, T.H., 1978. Present-day plate motions. J. Geophys. Res., 83: 5331–5354.

Minster, J.B., Jordan, T.H., Molnar, P. and Haines, E., 1974. Numerical modeling of instantaneous plate tectonics. Geophys. J.R. Astron. Soc., 36: 541–576.

Morgan, J.P. and Sandwell, D.T., 1994. Systematics of ridge propagation south of 30°S. Earth Planet. Sci. Lett., 121: 245–258.

Mougenot, D., Recq, M., Virlogeux, P. and Lepvrier, C., 1986. Seaward extension of the East African Rift. Nature, 321: 599–603.

Neumann, G.A., Forsyth, D.W. and Sandwell, D., 1993. Comparison of marine gravity from shipboard and high-density satellite altimetry along the Mid-Atlantic Ridge, 30.5°S–35.5°S. Geophys. Res. Lett., 20: 1639–1642.

Palmer, J., Sempéré, J-C., Christie, D. and Morgan, J.P., 1993. Morphology and tectonics of the Australian–Antarctic discordance between 123°E and 128°E. Mar. Geophys. Res., 15: 121–152.

Patriat, P., 1985. Reconstitution de l'évolution du système de dorsales de l'océan Indien par les methodes de la Cinematique des Plaques. Ph. D., Institut de Physique du Globe de Paris, 308 pp.

de Ribet, B. and Patriat, P., 1988. The axial region of the Southwest Indian Ridge between 53°E and 59°E: Evolution during the last 10 Ma. Mar. Geophys. Res., 10: 139–156.

Royer, J-Y. and Schlich, R., 1988. Southeast Indian ridge between the Rodriguez triple junction and the Amsterdam and Saint-Paul islands: Detailed kinematics for the past 20 m.y. J. Geophys. Res., 93: 13,524–13,550.

Royer, J.-Y. and Sandwell, D.T., 1989. Evolution of the eastern Indian Ocean since the Late Cretaceous: Constraints from Geosat Altimetry. J. Geophys. Res., 94: 13755–13800.

Royer, J.-Y. and T. Chang, 1991. Evidence for relative motions between the Indian and Australian plates during the last 20 Myr from plate tectonic reconstructions: Implications for the deformation of the Indo-Australian plate. J. Geophys. Res., 96: 11,779–11802.

Sandwell, D.T., 1992. Antarctic marine gravity field from high-density satellite altimetry. Geophys. J. Int., 109: 437–448.

Sclater, J.G., Dick, H., Norton, I.O. and Woodroffe, D., 1978. Tectonic structure and petrology of the Antarctic plate boundary near the Bouvet Triple Junction. Earth Planet. Sci. Lett., 37: 393–400.

Searle, R.C., 1986. GLORIA investigations of oceanic fracture zones: comparative study of the transform fault zone. J. Geol. Soc. London, 143: 743–756.

Sempéré, J-C., Palmer, J., Christie, D.M., Morgan, J.P. and Shor, A.N., 1991. Australian–Antarctic discordance. Geology, 19: 429–432.

Stewart, L.M., 1983. Strain release along oceanic transform faults. Ph. D. thesis, Yale University.

Tamsett, D. and Searle, R.C., 1988. Structure and development of the mid-ocean ridge plate boundary in the Gulf of Aden: Evidence from GLORIA side scan sonar. J. Geophys. Res., 94: 3157–3178.

Valenzuela, R.W. and Wysession, M.E., 1993. Intraplate earthquakes in the southwest Pacific ocean basin and the seismotectonics of the southern Tasman sea. Geophys. Res. Lett., 20: 2467–2470.

Wessel, P. and Smith, W.H.F., 1991. Free software helps map and display data. EOS, Trans. Am. Geophys. Union, 72: 441–446.

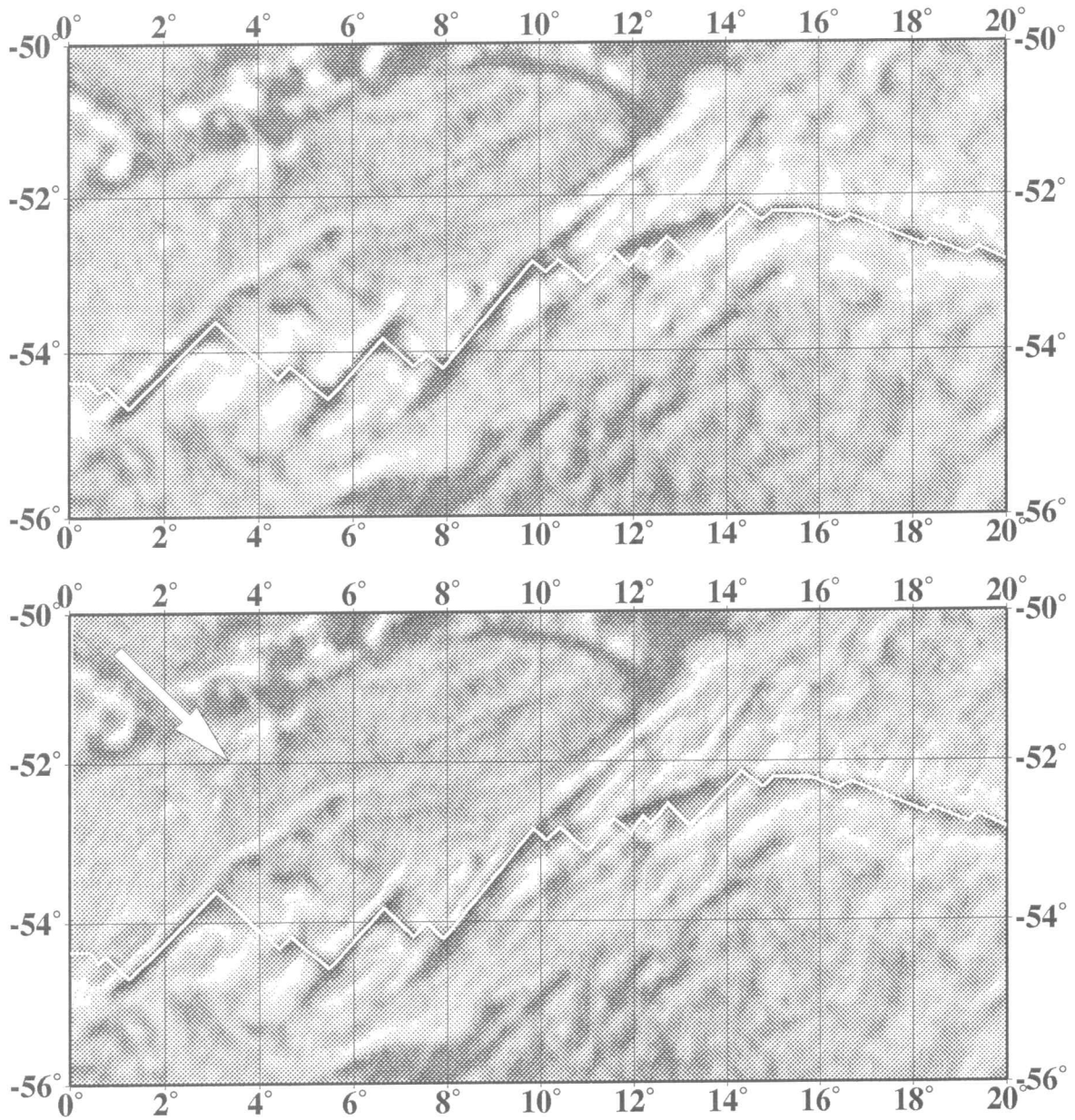

Fig. 6. Appendix 1. Upper: Free-air gravity anomalies from the Southwest Indian ridge, 0–20°E. Lower: For this and all subsequent figures, the white arrow specifies the direction of the derivative of the free-air gravity. This and all subsequent figures are Mercator projections.

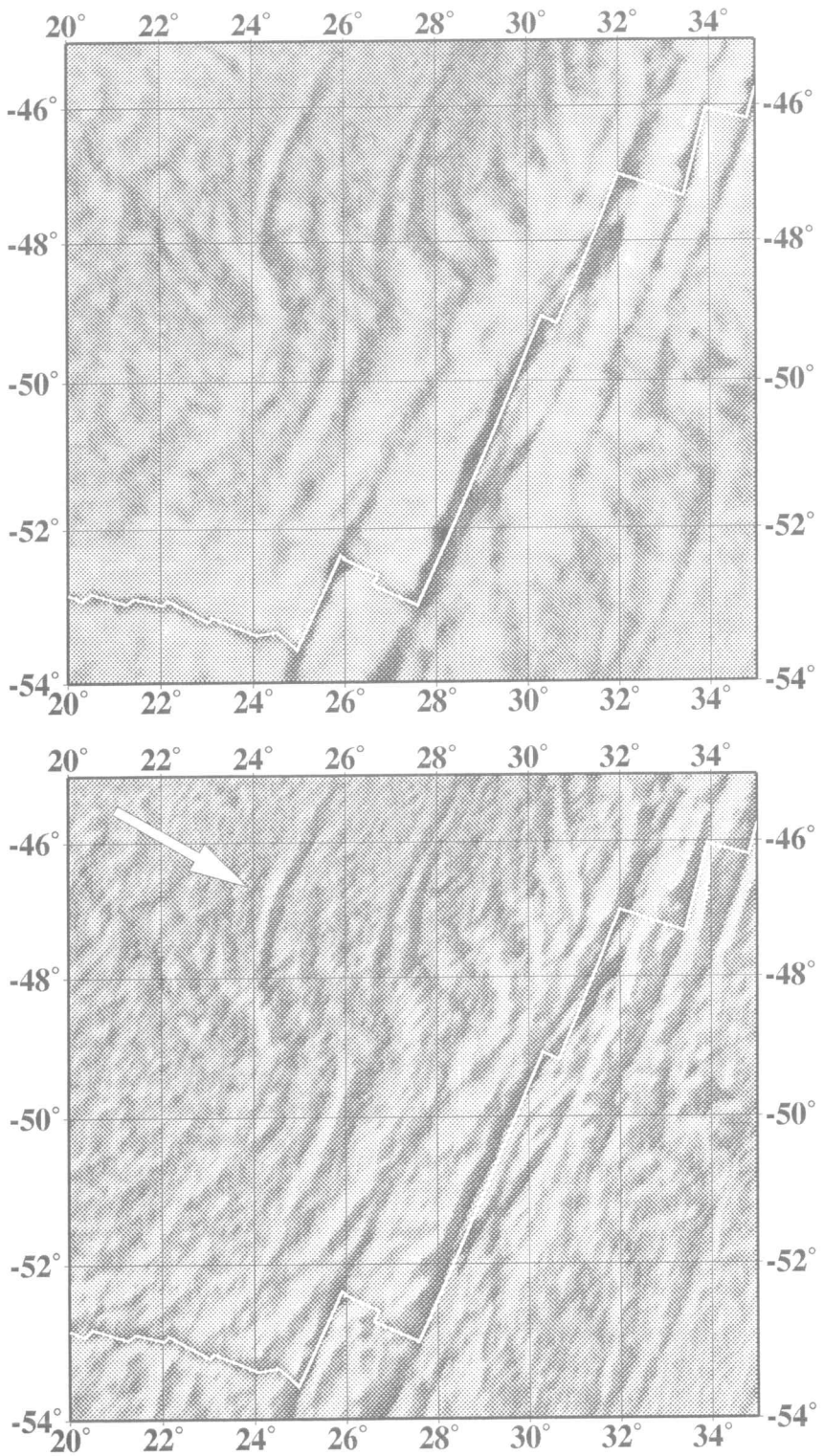

Fig. 7. Appendix 2. Upper: Free-air gravity anomalies from the Southwest Indian ridge, 20–35°E. Lower: Directional derivative of free-air gravity.

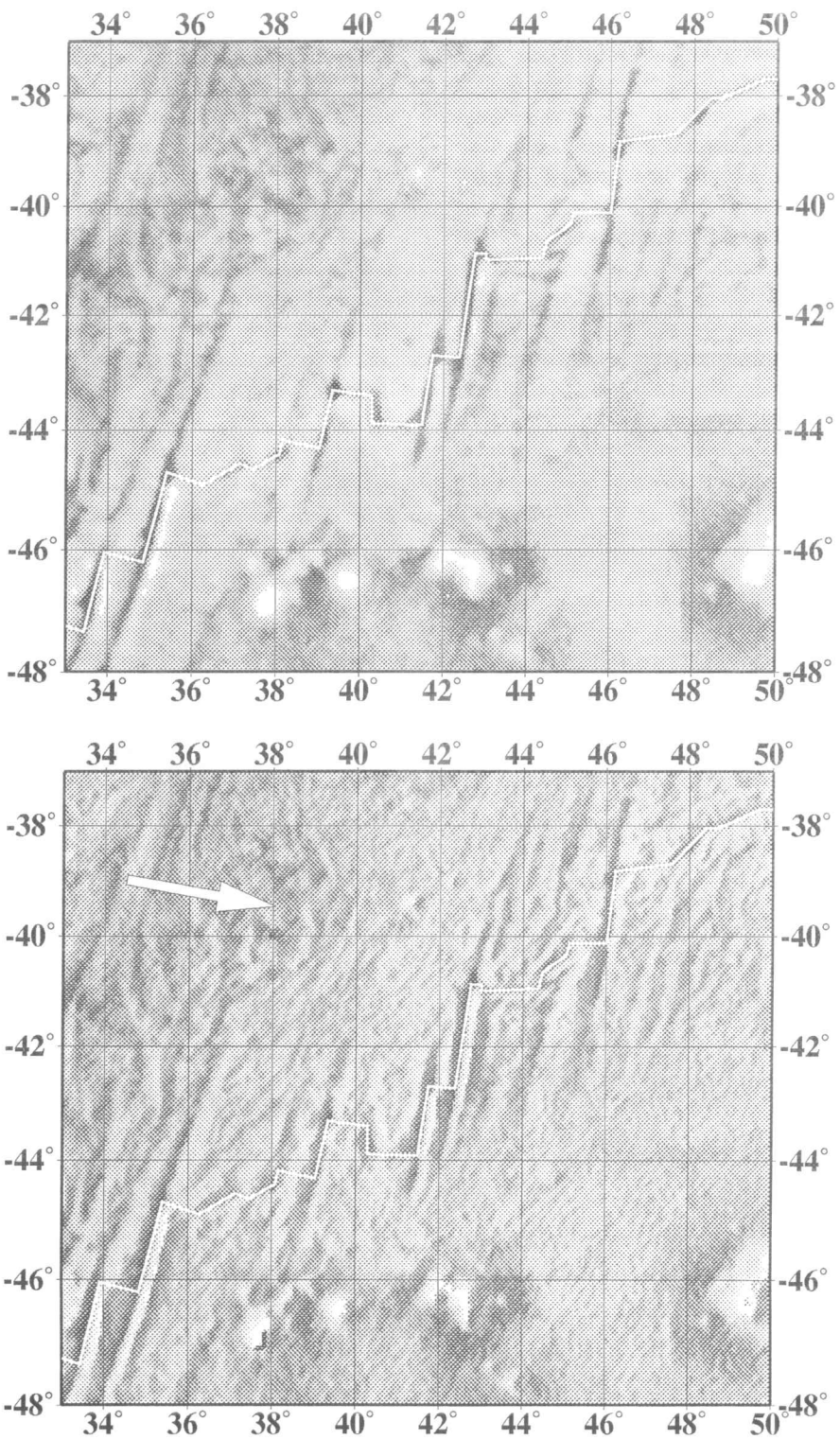

Fig. 8. Appendix 3. Upper: Free-air gravity anomalies from the Southwest Indian ridge, 33°–50°E. Lower: Directional derivative of free-air gravity.

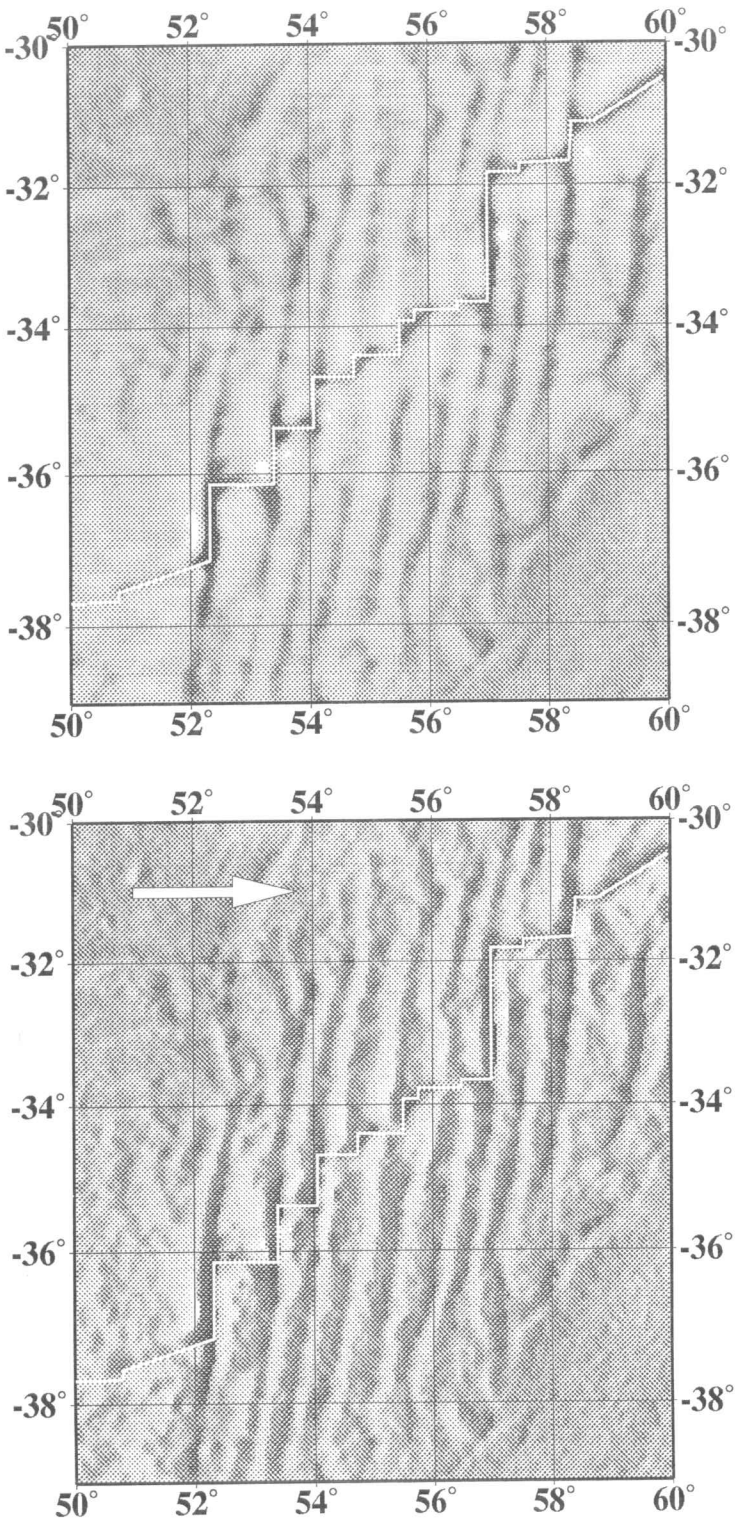

Fig. 9. Appendix 4. Upper: Free-air gravity anomalies from the western Southwest Indian ridge, 50°–60°E. Lower: Directional derivative of free-air gravity.

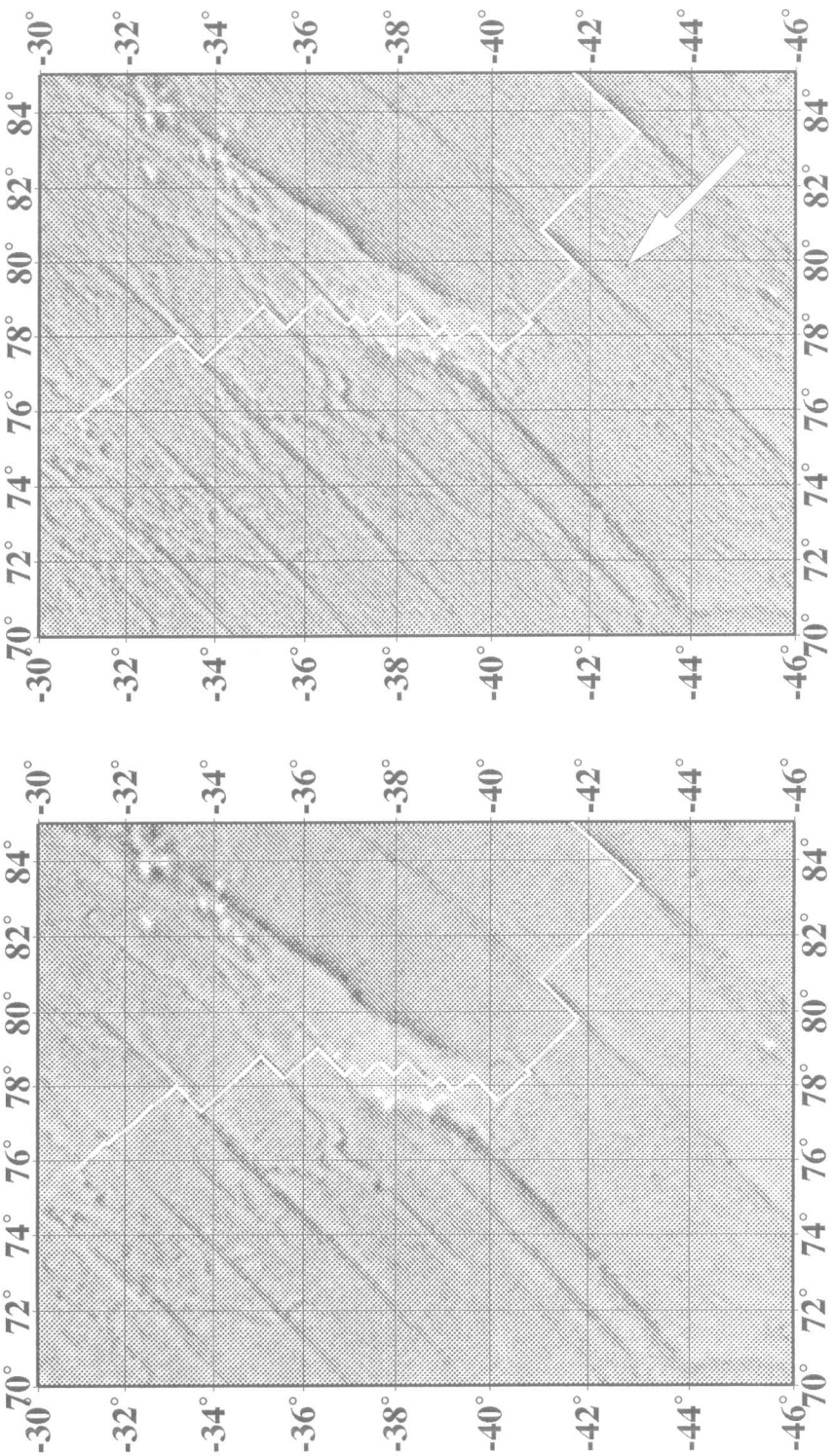

Fig. 10. Appendix 5. Left: Free-air gravity anomalies from the Southeast Indian ridge, 70°–85°E. Right: Directional derivative of free-air gravity.

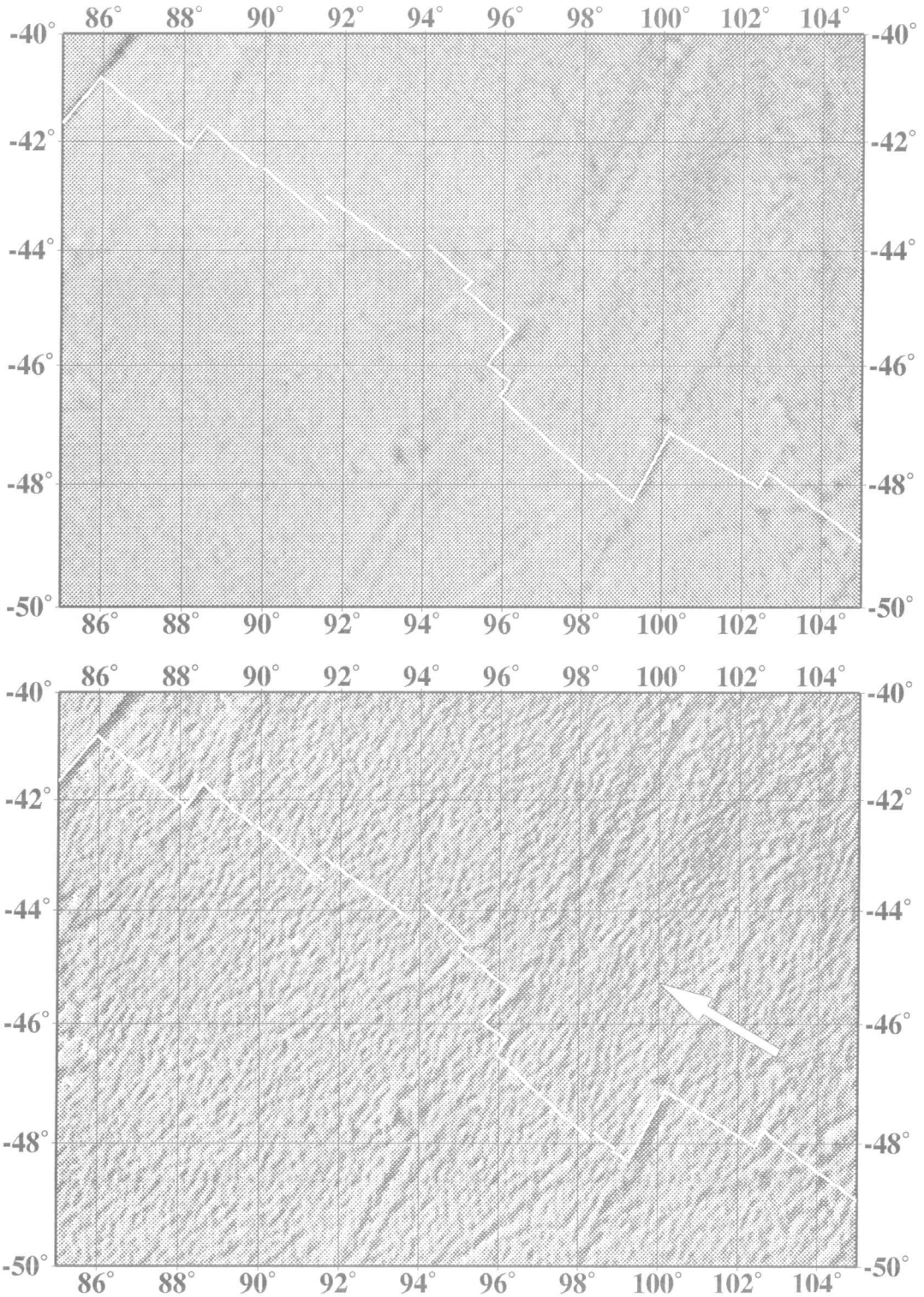

Fig. 11. Appendix 6. Upper: Free-air gravity anomalies from the Southeast Indian ridge, 85°–105°E. Lower: Directional derivative of free-air gravity.

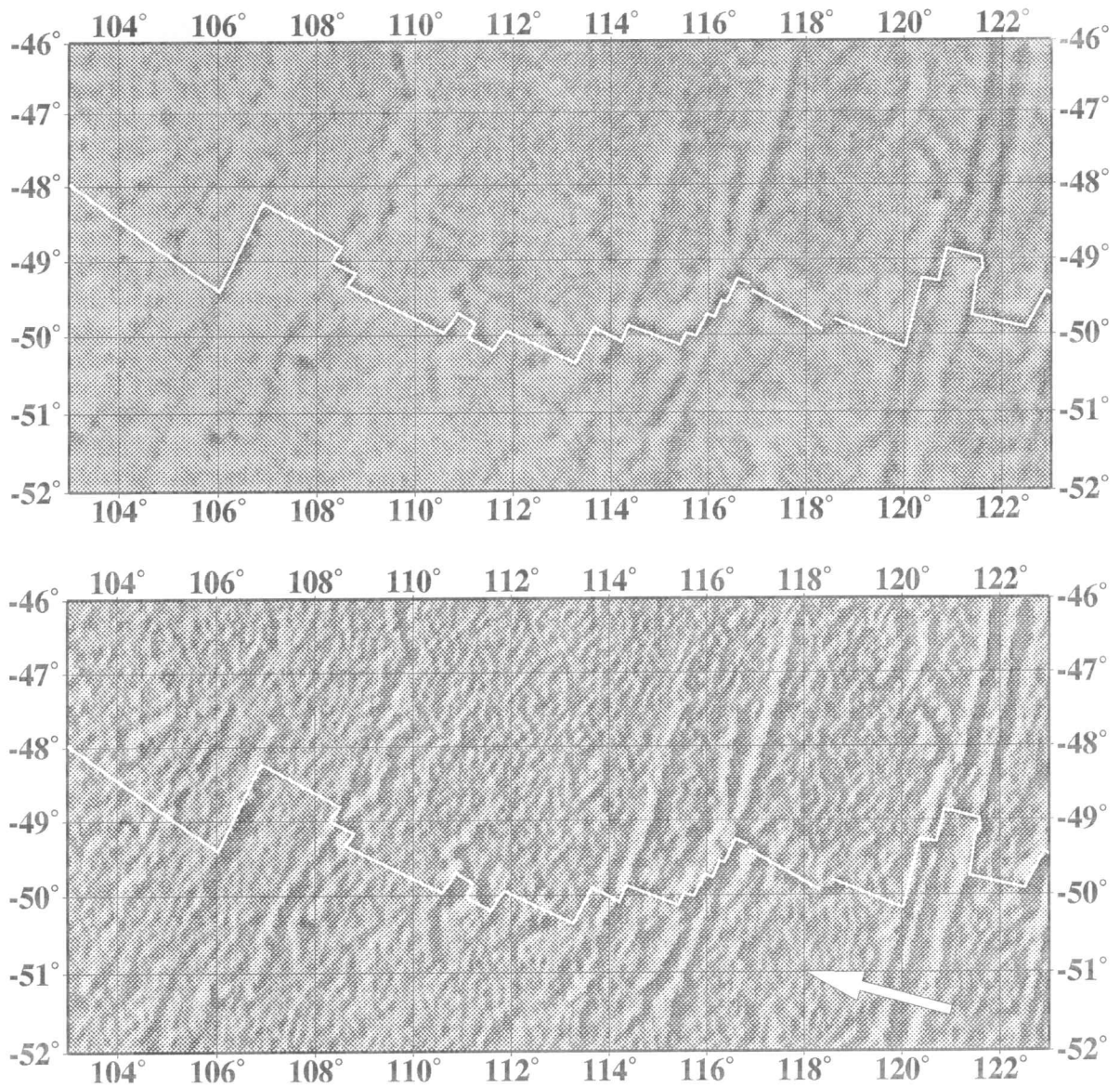

Fig. 12. Appendix 7. Upper: Free air gravity anomalies from the Southeast Indian ridge, 103°–123°E. Note that from 110°E to 120°E, transform fault orientations are hard to determine due to their small offsets and muted signature. Lower: Directional derivative of free-air gravity.

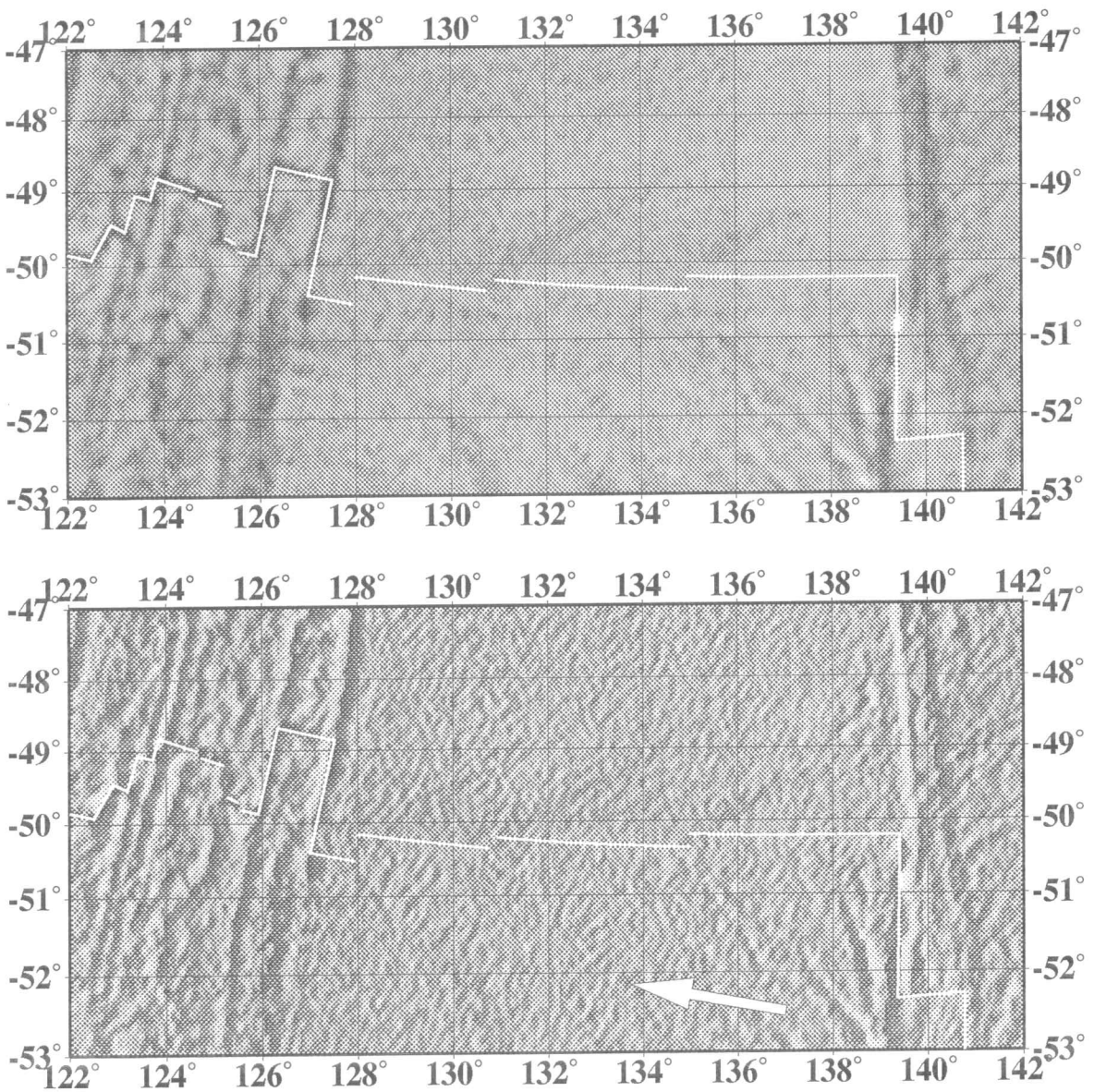

Fig. 13. Appendix 8. Upper: Free-air gravity anomalies from the Southeast Indian ridge, 122°–142°E. Lower: Directional derivative of free-air gravity.

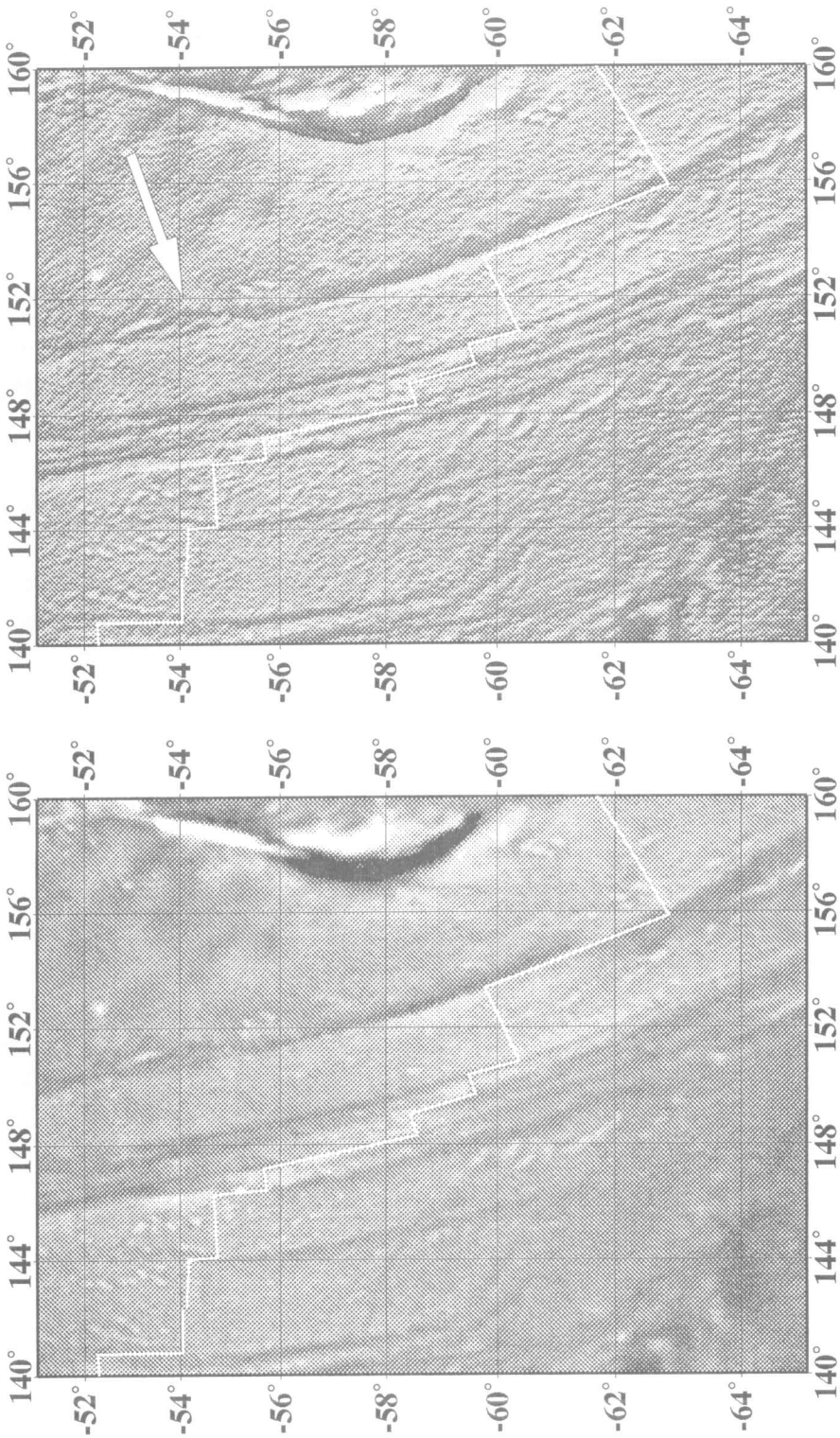

Fig. 14. Appendix 9. Left: Free-air gravity anomalies from the Southeast Indian ridge, 140°–160°E. Right: Directional derivative of free-air gravity.

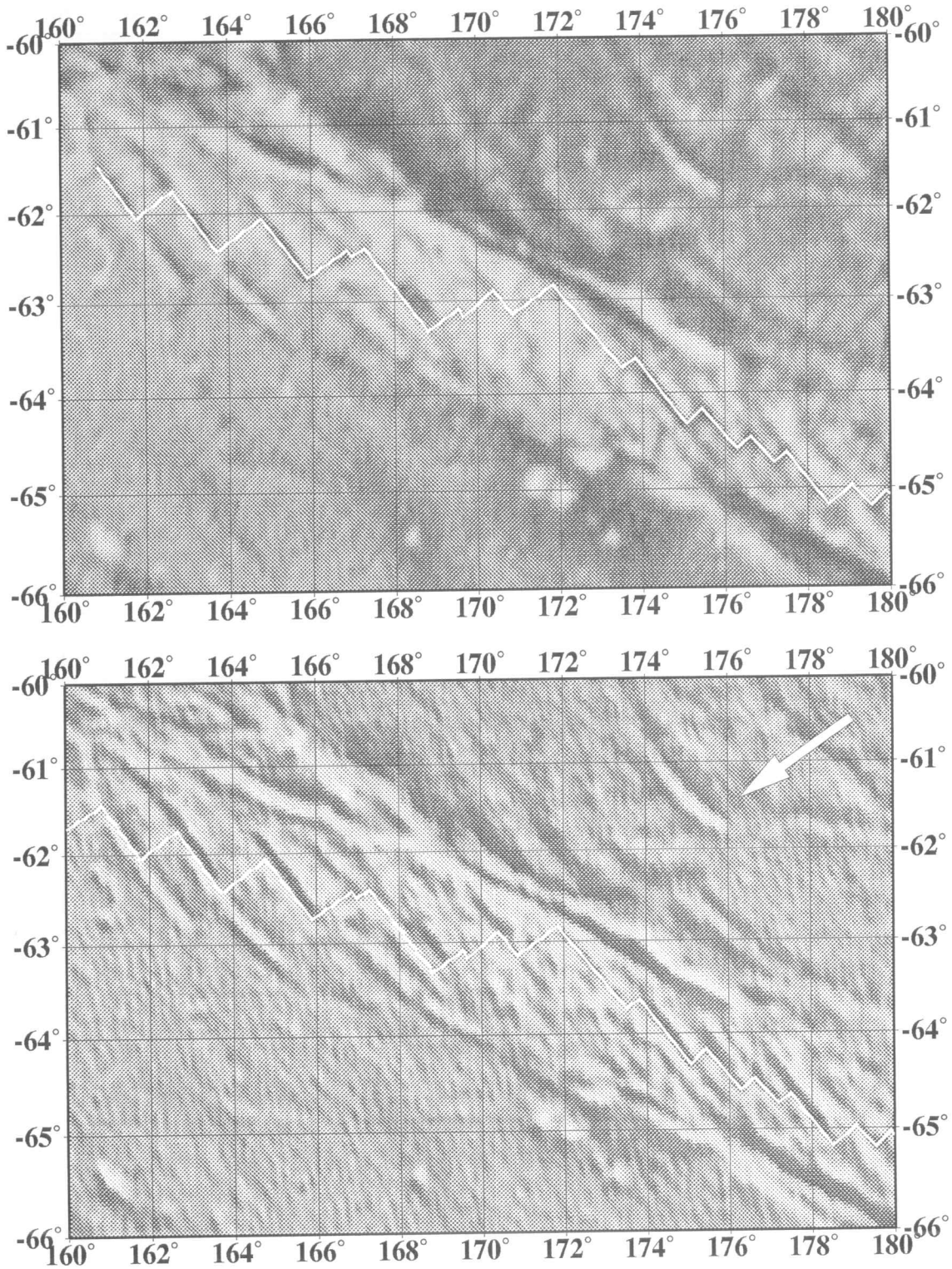

Fig. 15. Appendix 10. Upper: Free-air gravity anomalies from the Pacific–Antarctic rise, 160°–180°E. Lower: Directional derivative of free-air gravity.

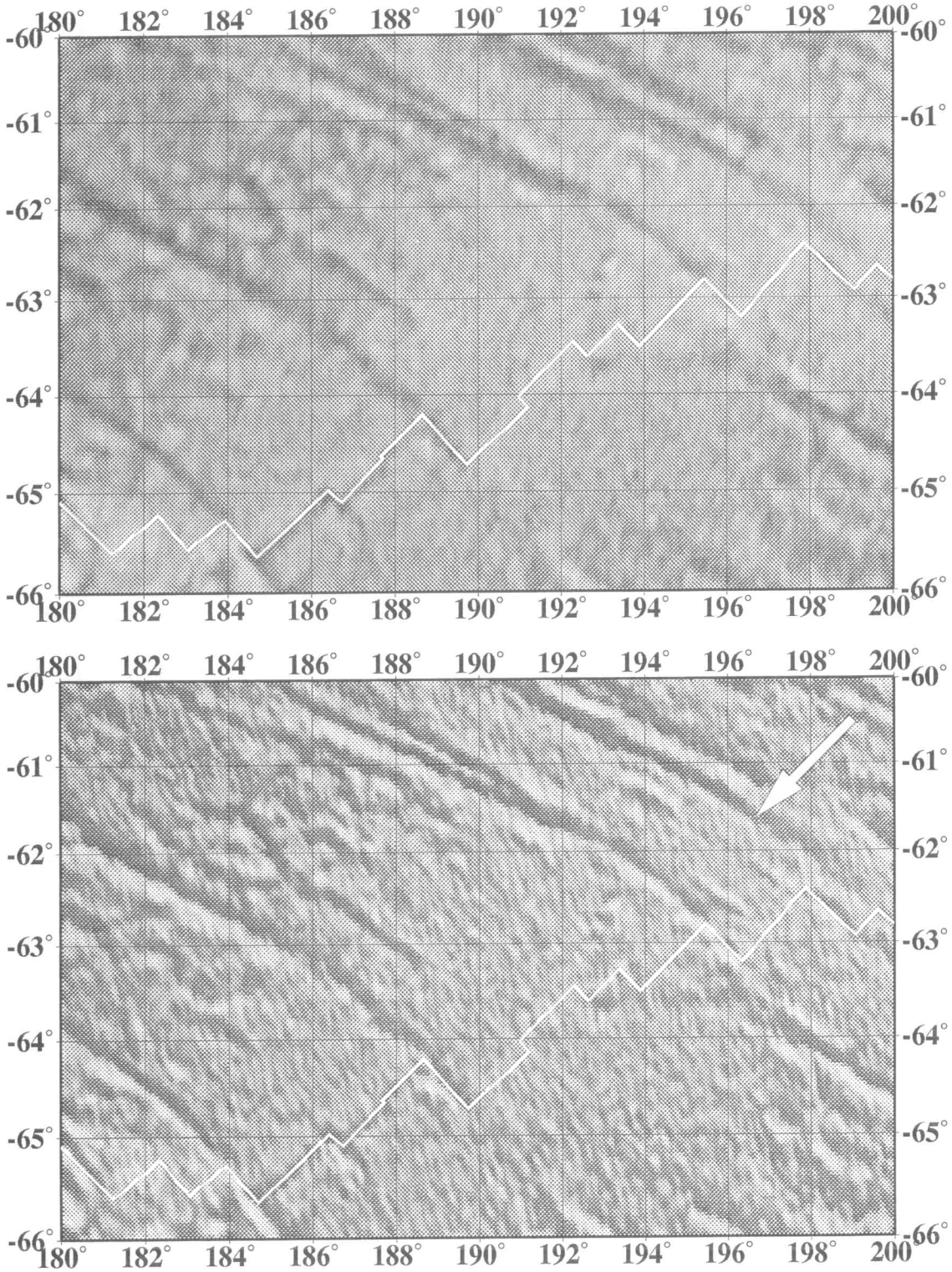

Fig. 16. Appendix 11. Upper: Free-air gravity anomalies from the Pacific–Antarctic rise, 180°–200°E. Lower: Directional derivative of free-air gravity.

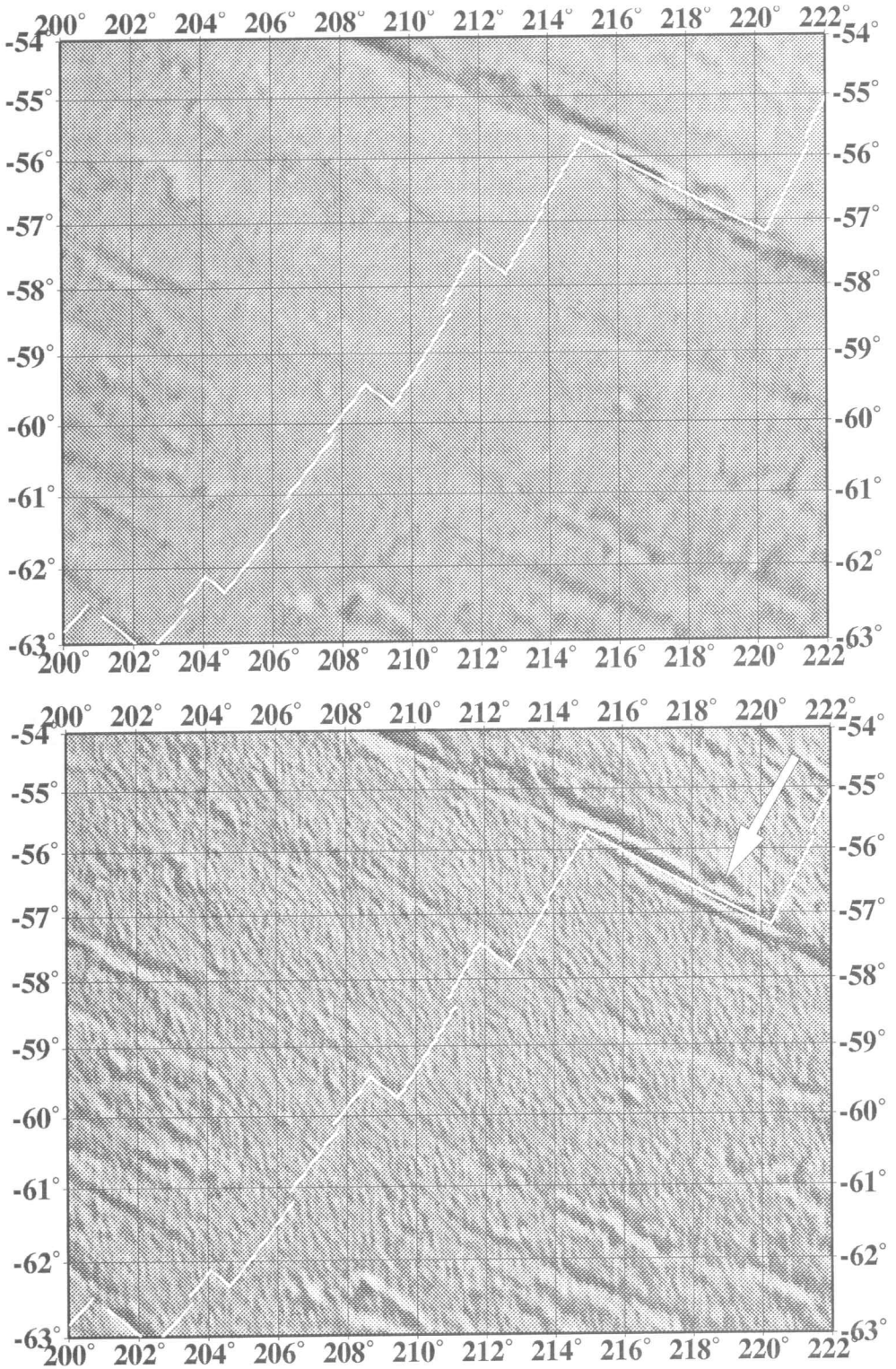

Fig. 17. Appendix 12. Upper: Free-air gravity anomalies from the Pacific–Antarctic rise, 200°–222°E. Lower: Directional derivative of free-air gravity.

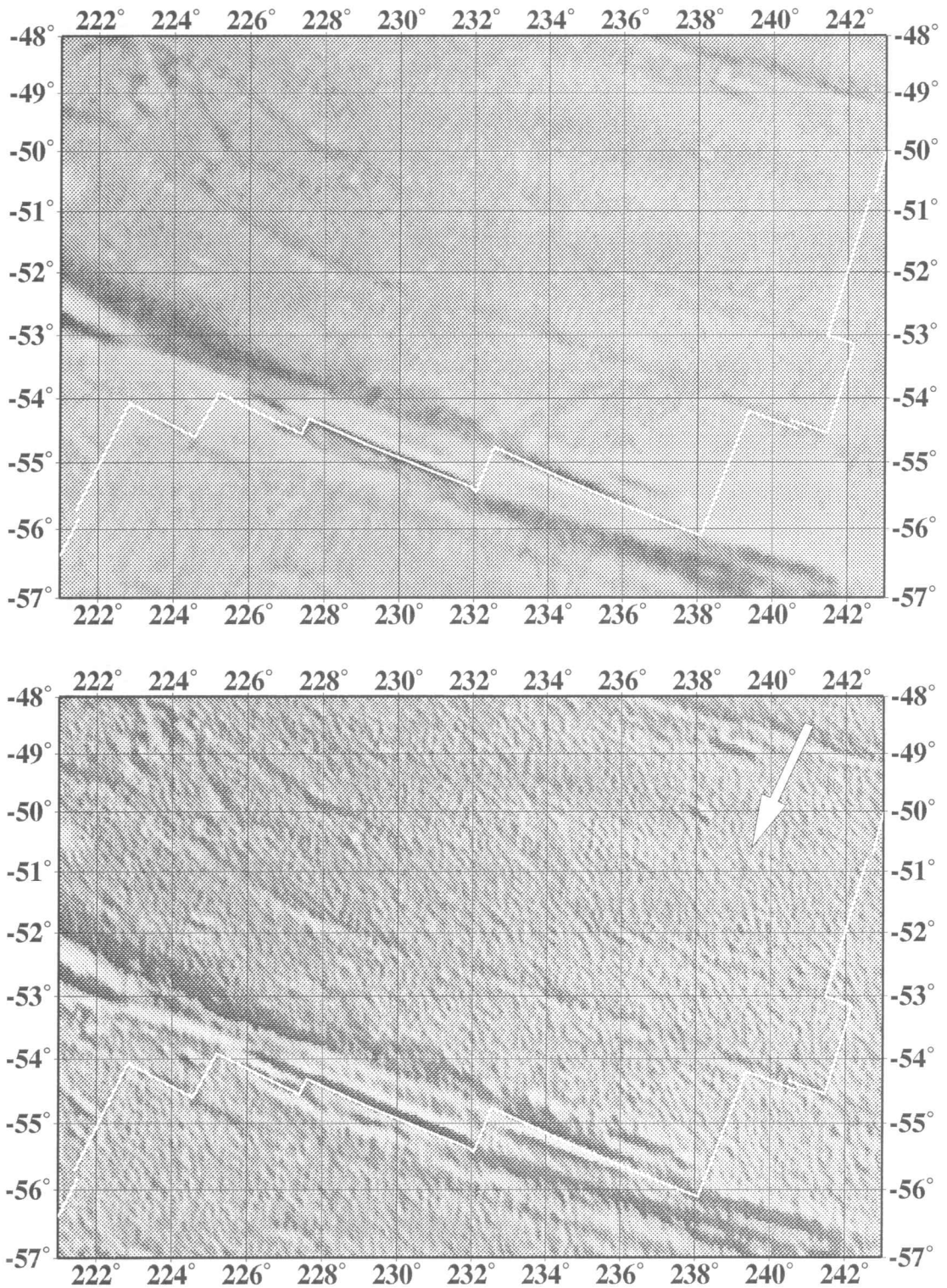

Fig. 18. Appendix 13. Upper: Free-air gravity anomalies from the Pacific–Antarctic rise, 221°–243°E. Lower: Directional derivative of free-air gravity.

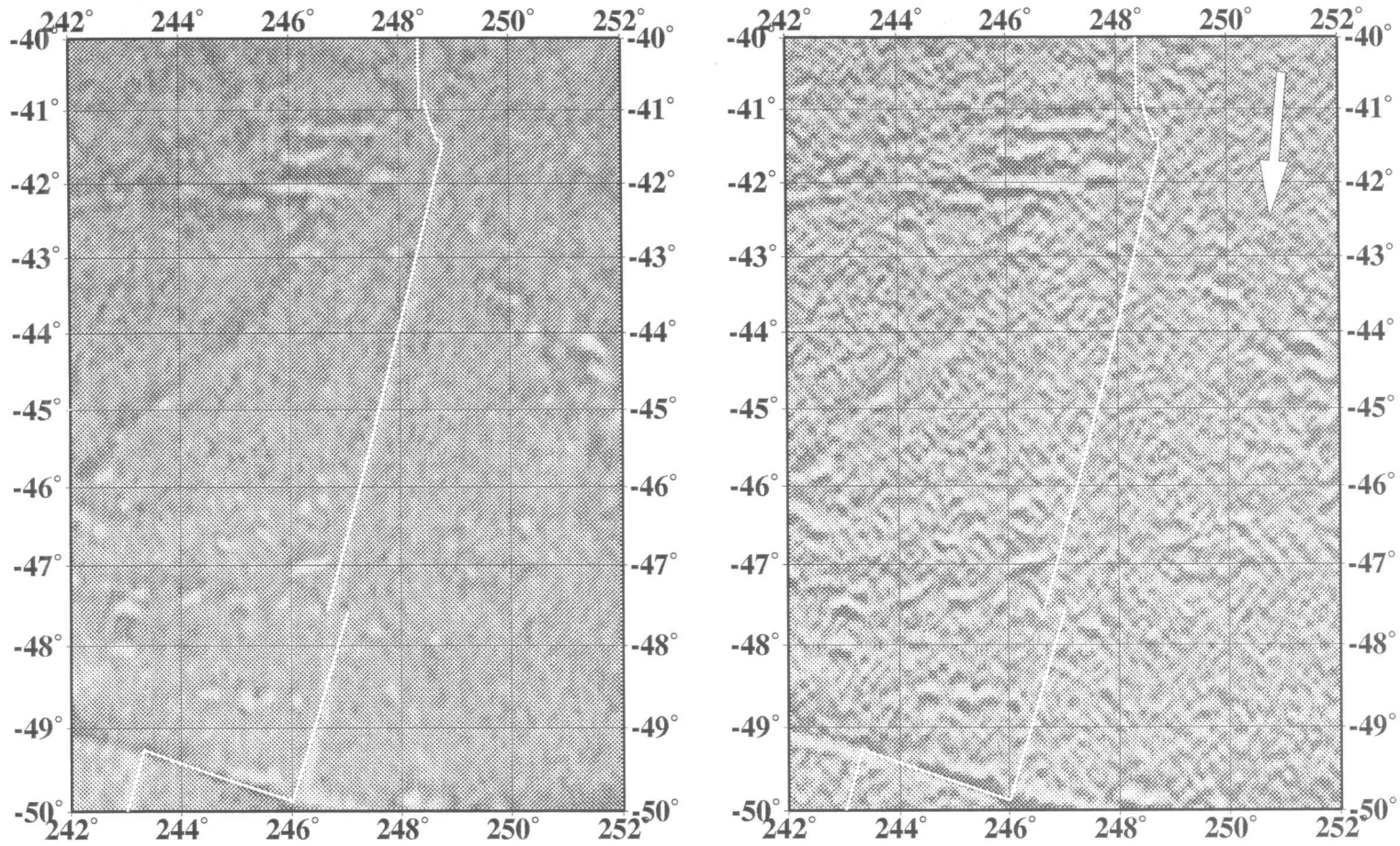

Fig. 19. Appendix 14. Upper: Free-air gravity anomalies from the Pacific–Antarctic rise, 242°–252°E. Lower: Directional derivative of free-air gravity.

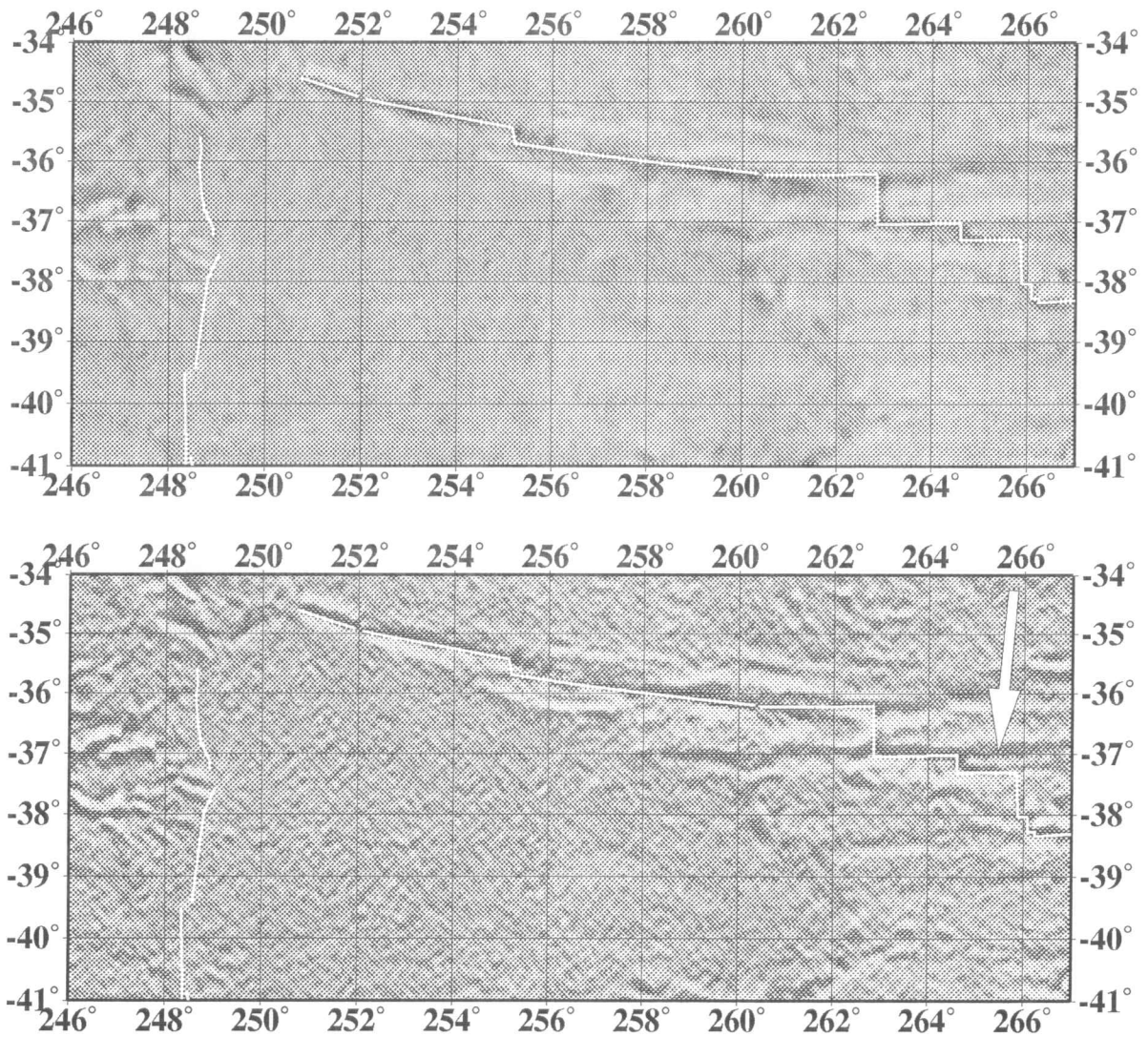

Fig. 20. Appendix 15. Left: Free-air gravity anomalies from the Chile rise and northern Pacific–Antarctic rise, 246°–267°E. Right: Directional derivative of free-air gravity.

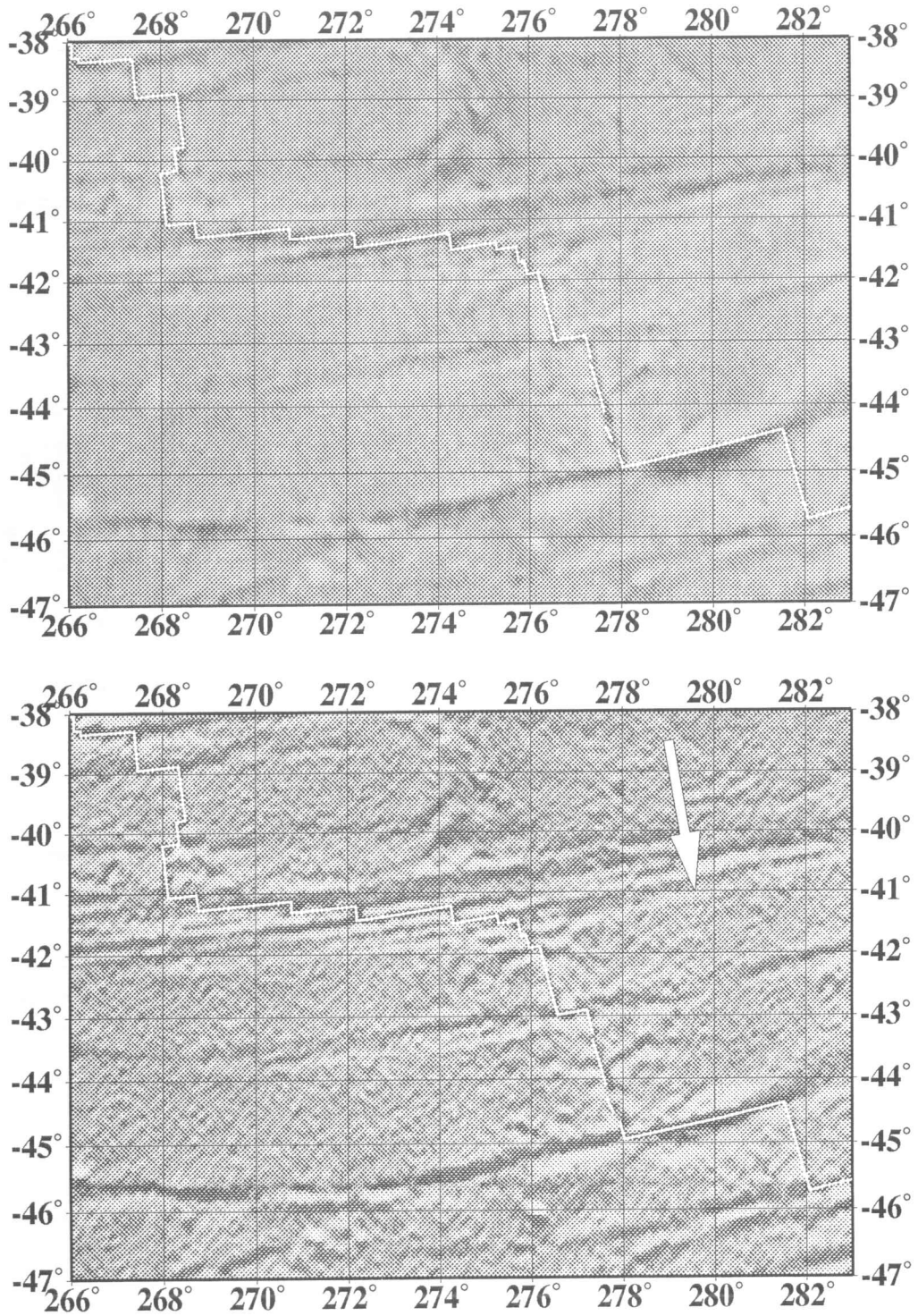

Fig. 21. Appendix 16. Upper: Free-air gravity anomalies from the Chile rise, 266°–283°E. Lower: Directional derivative of free-air gravity.

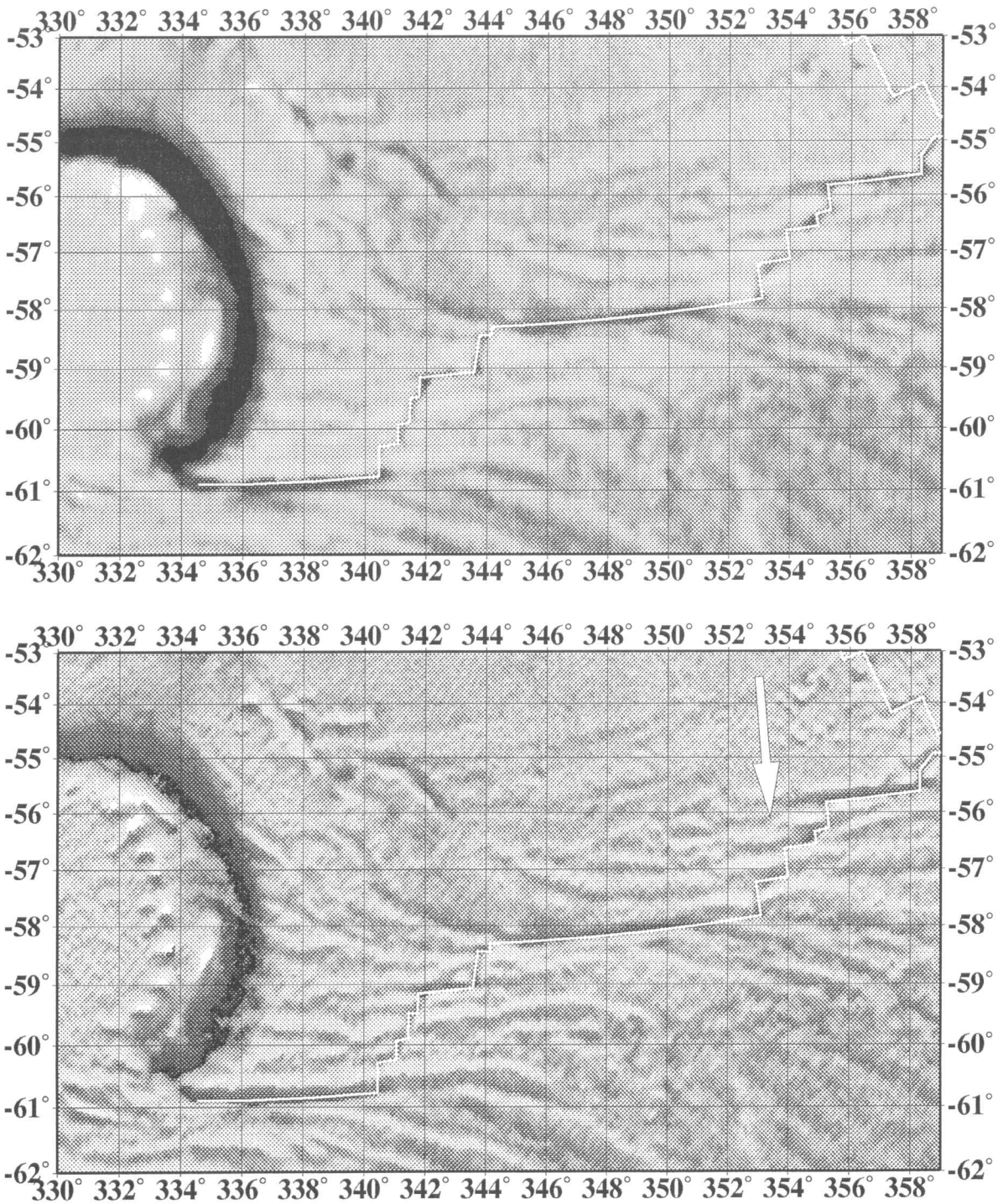

Fig. 22. Appendix 17. Upper: Free-air gravity anomalies from the America–Antarctic rise, 330°–359°E. Lower: Directional derivative of free-air gravity.

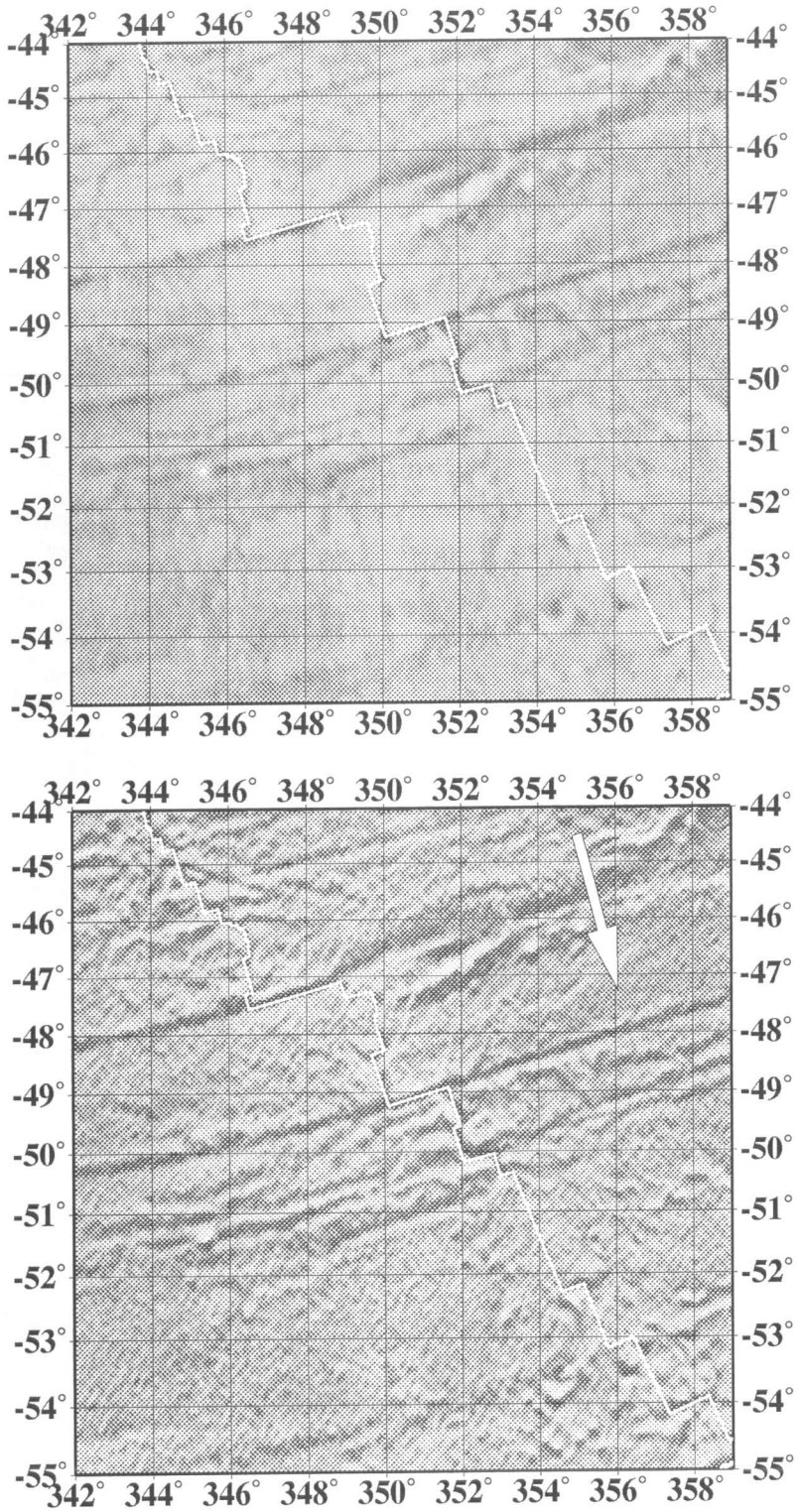

Fig. 23. Appendix 18. Upper: Free-air gravity anomalies from the southern Mid-Atlantic ridge, 44°–55°S. Lower: Directional derivative of free-air gravity.

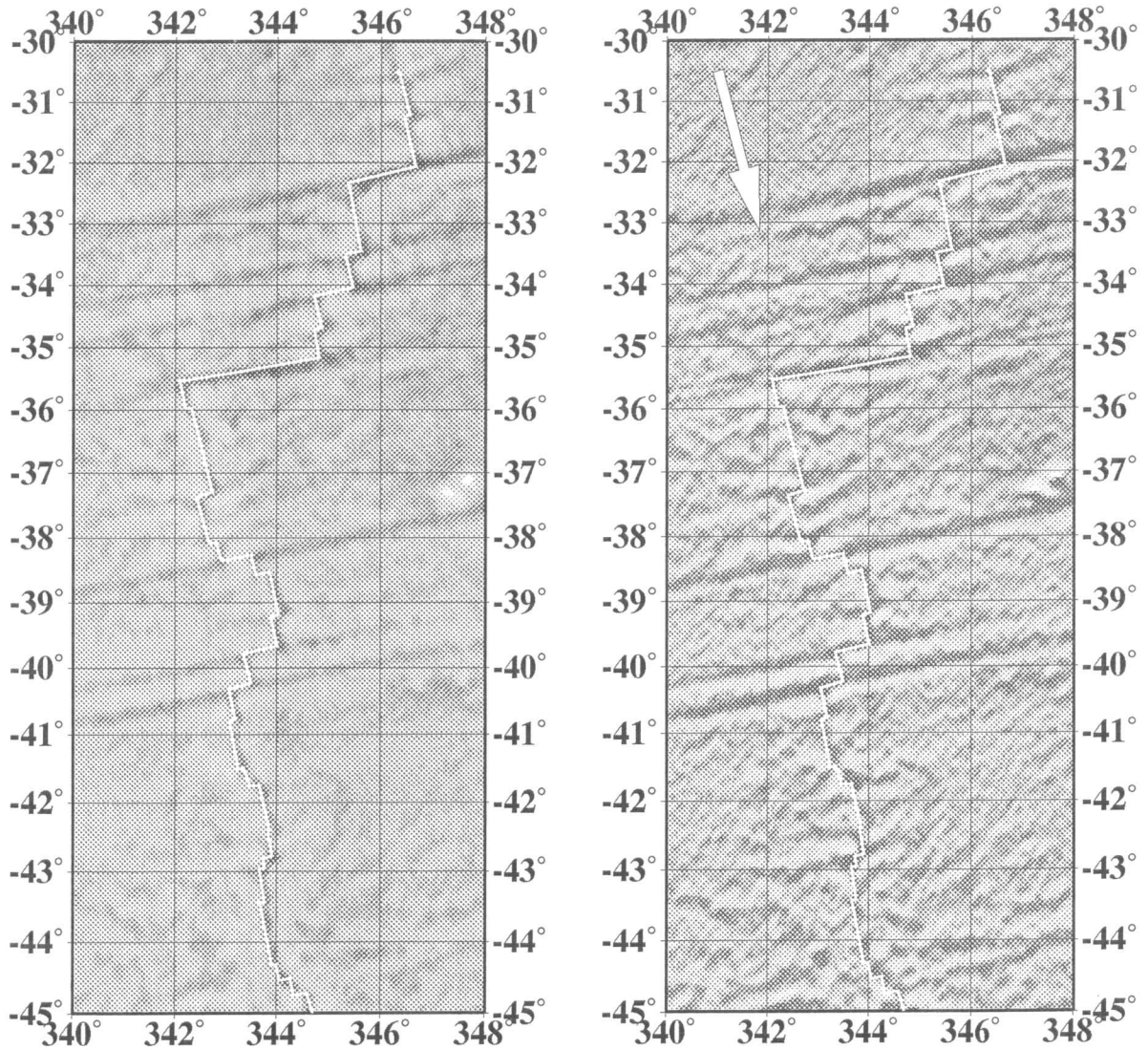

Fig. 24. Appendix 19. Left: Free-air gravity anomalies from the southern Mid-Atlantic ridge, 30°–45°S. Right: Directional derivative of free-air gravity.